Towards a Cryogenic Planar Ion Trap for Sr-88

by

Waseem Bakr

Submitted to the Department of Electrical Engineering and Computer Science
in partial fulfillment of the requirements for the degrees of

Bachelor of Science in Electrical Engineering and Computer Science

and

Master of Engineering in Electrical Engineering and Computer Science

at the

MASSACHUSETTS INSTITUTE OF TECHNOLOGY

June 2006

Author . . . . . .
Department of Electrical Engineering and Computer Science
May 24, 2006

Certified by . . . . . .
Isaac L. Chuang
Associate Professor
Thesis Supervisor

Accepted by . . . . . .
Arthur C. Smith
Chairman, Department Committee on Graduate Theses

Towards a Cryogenic Planar Ion Trap for Sr-88

by

Waseem Bakr

Submitted to the Department of Electrical Engineering and Computer Science
on May 24, 2006, in partial fulfillment of the
requirements for the degrees of
Bachelor of Science in Electrical Engineering and Computer Science
and
Master of Engineering in Electrical Engineering and Computer Science

Abstract

This thesis describes experiments with ion traps constructed with electrodes in a single two-dimensional plane, and ion traps operated in a cryogenic environment at 77K and 4K temperatures. These two technologies address needs which arise in developing potentially scalable approaches to quantum computing using trapped ions.

Traps with electrodes in a plane are challenging to load because their trap depths are usually only of order one percent that of multi-level traps of comparable dimensions. In addition, ion heating rates in these traps are higher than in multi-level traps because of the close proximity of the electrodes that is required to achieve a reasonable trap depth and the relatively resistive semiconductor electrode materials used in planar traps fabricated with standard semiconductor lithography methods.

We investigate planar traps using macroscopic ions, focusing on devising techniques for loading these shallow traps and designing electrode layouts for ion movement. Using traps fabricated lithographically with copper traces on fiberglass laminate, we trap linear chains of tens of charged particles of $\sim$ 400nm diameter. We perform experiments to address concerns about the low trap depth of planar ion traps and develop control electrode layouts for moving ions between trap zones.

Motivated by the desire to lower the heating rates in planar traps, we design and implement an experiment trapping Sr-88 ions in a knife-edge trap in a helium cryostat. The design challenges are obtaining a long hold-time of the cryogens, lowering the residual gas pressure and loading the trap using a technique compatible with the cryogenic environment. A novel loading technique we demonstrate successfully is laser ablation loading at 4K, employing a $SrCl_2$ target. Laser cooling is applied to produce observations of ions, both in clouds transitioning into Wigner crystals, and of linear chains of up to 14 optically resolved single ions. These results set the stage for future experiments with a planar trap for Sr-88 ions designed to operate at 4K.

Thesis Supervisor: Isaac L. Chuang
Title: Associate Professor

Acknowledgments

Over the past two years, my interaction with members of the Quanta group has been an enjoyable learning experience. I am grateful to every one of them for their mentoring, assistance and friendship.

I would like to thank Prof. Isaac Chuang for helping me become a better experimentalist. The opportunity he gave me to lead the work on the cryogenic ion trapping experiment has taught me valuable skills in experiment design and time management. I am also grateful for his efforts to improve my scientific communication skills and I hope they are reflected in this work.

I would also like to thank Ken Brown, our post-doc, for his continuous support throughout my stay with the group. He has been generous with his advice whenever I faced experimental difficulties and brilliant in his explanations of theoretical concepts in atomic physics. I wish him a prosperous career in his new position as a professor at Georgia Tech.

Paul Antohi, who is taking over the cryogenic experiment, has been a great collaborator and I trust he will use the apparatus to produce several important results in coming years.

I thank Rob Clark for his sense of humor and good taste in music, Jarek Labaziewicz for his constant stream of bright ideas and Chris Pearson for his mechanical engineering genius and patient mentoring. I also thank Dave Leibrandt for teaching me how to methodically approach a research problem.

Finally, I warmly thank my parents for their love and encouragement, and their support of my decision to pursue a career in physics.

Contents

List of Figures

Chapter 1

Introduction

Over the past thirty years, trapped ions have become an invaluable tool of the atomic physicist, finding a wide range of applications including frequency standards [Fis97], mass spectroscopy [Tod91] and precision spectroscopy [IBW87]. A trapped ion provides an excellent realization of an elementary quantum system that is very well isolated from environmental noise and yet easily controllable using interactions with laser fields. It is precisely this feature that makes ion traps a good candidate for quantum computation, an idea first proposed in 1995 by Cirac and Zoller [CZ95].

The basic building blocks for an ion trap quantum information processor are now available [WMI+98, BZ88, NLR+99, TWK+98], but it is clear that a scalable ion trap quantum computer (ITQC) will require rethinking traditional trap designs. In addition, decoherence rates in current ion traps are higher than acceptable for scalable quantum computation. However, if these rates are pushed down low enough, fault tolerance threshold theorems promise that an ITQC would perform reliably even with faulty components once component error probabilities fall below a certain hardware-dependent threshold, typically around 10^{-4} [Pre99, MCT+04].

This work investigates cryogenic planar ion traps which directly address both of the problems raised above; the lack of scalability and high decoherence rates of current ITQCs. We demonstrate the recently proposed planar design [CBB+05] by trapping macroscopically charged particles above electrodes in a printed circuit board. This planar design is potentially scalable to many-zone traps and is amenable to modern

microfabrication techniques. We also load strontium ions into a knife-edge trap at liquid helium temperature using a novel laser ablation techniqe and resolve chains of single ions in the trap. Recent experiments suggest [DOS+06, PBIW96] that the cryogenic environment we put our trap in could possibly reduce heating rates due to noise from the trap electrodes and residual gas collisions.

The rest of this chapter is structured as follows. First, we briefly review trapped-ion quantum computation, the long-term motivation for this work. We describe the Cirac-Zoller scheme for computing with trapped ions and one proposed architectures for scaling it up. We then introduce planar traps and cryogenic traps as technologies that have the potential to be very useful in this scaling process. We review previous proposals and experiments related to these technologies that served as an inspiration for our work, as well as the challenges in implementing these technologies, some of which this thesis addresses. Finally, we summarize our main results and contributions, providing pointers to relevant chapters in this thesis document, and place our work in perspective with respect to an eventual goal of trapping ions in microfabricated silicon traps.

1.1 Ion trap quantum computation

Quantum mechanical phenomena, such as superposition and entanglement, may be utilized in a physical system, such as an ion trap, to perform computation [Fey82, Deu85]. Quantum computers are able to solve certain problems polynomially, and in some cases exponentially, faster than their classical counterparts. Shor's discovery of a quadratic time factoring quantum algorithm [Sho99] has generated a lot of interest in experimental realizations, including ion traps, nuclear magnetic resonance [GC98], cavity QED [CZKM97], quantum dots [LD98] and others.

An implementation of an ITQC addresses all five of the DiVincenzo criteria [DiV00] for the physical implementation of a quantum computer. Optical or hyperfine states of the ions provide the qubits and can easily be initialized in the ground state. Experimentally measured coherence times of hyperfine qubits exceed ten minutes [FSL+95],

limited mainly by magnetic field perturbations. Qubit readout can be easily accomplished via state-sensitive light scattering. Single qubit rotations are achieved by using laser or microwave radiation to couple the two levels of a qubit for a specific period of time. Finally, performing two qubit gates is a little trickier and is the essence of the Cirac-Zoller proposal outlined below.

1.1.1 The Cirac-Zoller proposal

In the proposed scheme, a chain of ions is confined in a harmonic potential in three dimensions produced by a linear trap. The ions are lined up in the z direction in which the confinement is much weaker than the radial directions. Sideband cooling is used to put the ions in the motional ground state with high probability.

The ions can interact with standing electromagnetic waves. We assume the Lamb-Dicke limit and low laser intensities so that only the center of mass mode of the ions can be excited. To focus on the evolution due to the laser interaction, we use the interaction picture where the Hamiltonian for the nth ion is

$$H_n \propto |e\rangle_n \langle g| \, a e^{-i\phi} + |g\rangle_n \langle e| \, a^\dagger e^{i\phi}. \tag{1.1}$$

The states $|g\rangle$ and $|e\rangle$ are the ground and excited internal states of the ion, a and $a^\dagger$ are the standard annihilation and creation operators for the harmonic oscillator and ϕ is the phase of the laser.

The key idea for performing two-qubit gates is to use the center of mass mode as a bus for transferring information between ions. Suppose we want to perform a controlled phase gate between ions i and j, where i is the target and j is the control. We first aim the laser at i to map its internal state onto the bus. There are two possible scenarios: (1) i is initially in $|g\rangle$, in which case, this and subsequent steps have no effect or (2) i is initially in $|e\rangle$ and a phonon is created on the bus, while i flips to state $|g\rangle$. We assume the more interesting case (2) for the rest of this description. Next, we aim the laser at j to perform an entangling gate between the motional state and internal state of j. The system gains a phase conditioned on the internal state of

j. Finally, we repeat the first step to return the system to its original state modulo the phase gained. The overall result is that the system accumulates a phase only if both ions start out in the excited state.

The controlled phase gate above can easily be converted to a CNOT gate, and it is well-known that the single-qubit gates and CNOT are a universal set of gates for quantum computation [NC00].

1.1.2 Scalable architectures

Although the scheme described above is implementable with a few ions, it is hard to scale up. It is technically difficult to manipulate a large number of ions in a single trap. In 2002, Kielpinski *et al* [KMW02, WMI+98] suggested a scalable architecture consisting of a large number of interconnected traps. DC voltages applied to segmented trap electrodes shuttle ions between different trapping zones. Ions are normally stored in a memory region, and are moved to an interaction region when we need to perform logic gates on them.

The basic elements of this scheme have all been experimentally demonstrated; state readout [BZ88], one and two qubit gates [NLR+99, TWK+98], and ion shuttling in straight lines and through tees [R+02, H+05]. Scaling this architecture up to the many thousands of qubits necessary for a useful computation, however, will involve significant physics and engineering challenges.

The ion traps used for quantum computation are based on the linear RF Paul trap [PDM89, Pau90, RGB+92, Gho95]. Current experiments typically use gold electrodes deposited on two or more alumina substrates with a geometry similar to that shown in Figure 1.2(a) [T+00, DHL+04]. While these multi-level traps can be adapted to microfabrication techniques [MHS+04], it is not clear whether they can be scaled to many zone traps because they require slots through the trap structure. This will make trap topologies that include loops difficult, as there will be islands of electrodes that will have to be mechanically supported and electrically connected. In addition, the precise alignment of the electrodes in the different levels is very challenging.

One solution to the problems above is a trap with all the electrodes in one plane,

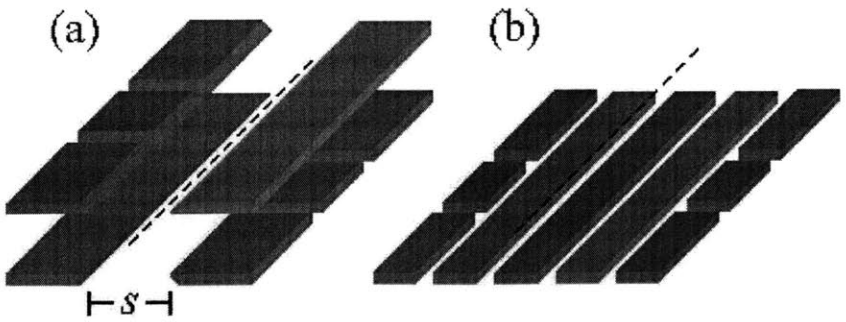

Figure 1-1: Schematic illustrations of (a) a two-level linear RF Paul trap representative of what is currently used in quantum computation experiments, and (b) the five electrode planar ion trap suggested by Chiaverini et al. [CBB+05]. Ions are trapped along the trap axis, shown as a dotted line. An RF potential is applied to the red electrodes to provide radial confinement, and DC potentials are applied to the blue control electrodes to provide axial confinement and to shuttle ions along the trap axis. Typical dimensions for current two-level traps are a slot width s of 200-400 μm. Figure taken from [PLB+06].

described in the following section.

1.2 Planar traps

In 2005, Chiaverini et al. [CBB+05] proposed using a planar RF Paul trap geometry for ion trap quantum computing which is easy to scale up to many zone traps and amenable to modern microfabrication techniques. The electrodes all lie in a plane and ions are trapped above the plane of the electrodes [JPM90]. In the five electrode planar trap design shown in Figure 1.2(b), the center and outermost electrodes are held at RF ground while the remaining two electrodes are biased with an RF potential for radial confinement. Either the center electrode or the outermost two electrodes can be segmented and DC biased for axial confinement. Such planar ion traps can be built using silicon VLSI technology and thus have the capability to scale to arbitrarily large and complex trap arrays [K+05]. In addition, CMOS logic can be integrated into the chip for controlling DC voltages for ion shuttling.

Several challenges will have to be addressed, however, before planar ion traps can

be used for quantum computing. Perhaps the most significant challenge is that planar ion traps have trap depths that are only of order 1 percent that of a multi-level trap of comparable dimensions [CBB+05]. While this is not a problem once the ions are loaded and laser cooled to near the ground state of the motion, it makes loading from a thermal ion source at room temperature or above difficult. Another challenge is that ion heating is enhanced first by the close proximity of the electrodes that is required to achieve a reasonable trap depth, and second by the more resistive semiconductor materials used for VLSI [LYS05]. Finally, optical access for laser cooling is blocked along the axis orthogonal to the trap substrate.

The first two challenges are topics that will be addressed in this work. We shall describe methods for increasing the depth of planar traps and loading low energy ions using non-traditional techniques such as loading from a four-rod trap or loading ions produced by laser ablation. Cryogenic trapping, described in the next section, is likely to dramatically reduce heating rates.

1.3 Cryogenic traps

In this section, we briefly outline some of the motivations for building a cryogenic ion trap and describe previous work in this direction.

1.3.1 Motivations for cryogenic trapping

Collisions with background gas molecules cause decoherence of the quantum information [Kie96]. Collisions also cause ion loss either by knocking ions out of the trap or chemically reacting with them. Because of this, ultra-high vacuum pressures are necessary in ion trapping. The UHV environment in an ion trap apparatus is usually achieved using room temperature vacuum pump technologies such as ion pumps which are able to achieve base pressures in the 10^{-10} to 10^{-12} torr range. At these pressures, the choice of materials used in trap construction is severely limited because outgassing from most materials creates virtual leaks [Els75]. Even when the proper vacuum compatible materials are used, the trapping apparatus still needs to be baked

for a long time, usually between one and two weeks.

Besides collision-induced decoherence, ion heating is another factor that limits gate fidelity. Measurements of the dependence of heating rates in ion traps on trap dimensions [TWK+98] reveal that the heating rates are dominated by a source other than Johnson noise that has been named "anomalous heating". Preliminary results from experiments where the trap electrodes have been cooled to liquid nitrogen temperature (77K) indicate that anomalous heating rates are significantly reduced at such temperatures, possibly even to the extent where the more well-understood temperature-dependent Johnson noise is the dominant contributor to the heating rate [DOS+06].

In the cryogenic setup described in this work, a radiofrequency trap is placed inside a vacuum tight container attached to the cold plate of a helium cryostat. At 4K, residual gases cryopump to the trap electrodes, the container walls and any other surfaces in thermal contact with the cold plate. Pressures as low as 10^{-17} torr have been reported in similar setups [G+91]. The low temperature is also expected to reduce anomalous and Johnson heating significantly. Finally, because outgassing is no longer a problem at 4K, baking the apparatus is not needed and the choice of materials that can be used in the trap construction encompasses a larger set of materials, including non-UHV-compatible ones such as plastics.

1.3.2 Previous work

Several workers have successfully built cryogenic ion traps. The NIST ion storage group has trapped $^{199}Hg^+$ ions in a linear RF trap at liquid helium temperature for use as a frequency standard at 40.5 GHz [PBIW96]. The high vacuum was needed to reduce ion loss and frequency shifts due to background gas collisions and shifts due to blackbody radiation. Okada *et al* used a similar setup to trap unstable Be^+ isotopes to study the Bohr-Weisskopf effect [OWN+02].

Other kinds of traps have also been used in cryogenic environments. Willems and Libbrecht have used the lifetime of cesium trapped in a magneto-optical trap placed in a continuous-flow helium cryostat to estimate the background pressure they achieve at 4×10^{-12} torr [WL95]. Penning ion traps operated at 4K have been used to load

and cool antiprotons via collisions with cold electrons to perform extremely accurate measurements of the antiproton inertial mass [G+91].

The cryogenic trap described in this work is most similar to the NIST trap, although there are some differences. The most important of these are the use of $^{88}Sr^{+}$ instead of $^{199}Hg^{+}$ and the use of ablation to load the trap instead of an oven/e-gun system.

1.4 Overview of this work

The specific research questions considered, the main results of this work, together with pointers to the relevant sections of this thesis document are summarized in the table below.

Research questions	Result	Section
What techniques can be used for loading planar traps given their low trap depths compared to multi-level traps of similar dimensions? How do we design a rapid development test bed for accurately simulating atomic ions in planar traps?	Loaded a printed circuit board planar trap with macroscopic ions via an intermediary four-rod trapping stage with a higher trap depth. Increased the depth of the planar trap by using a positively biased conducting plane above it. Measured the trap's secular frequencies and the height of the ions above the substrate, finding good agreement with simulations.	2.1, 2.3.1, 2.3.2
What electrode layouts and voltage sequences minimize the probability of ion loss while performing movement operations in ion traps?	Demonstrated basic movement operations in a planar trap using macroscopic ions in a rough vacuum (15 Pa.) For achieving similar results with atoms, the electrode layouts and voltage sequences used for macroscopic ions will have to scaled and further modified to take into account reduced motional damping in the absence of a buffer gas.	2.2.2, 2.3.3

Research questions	Result	Section
How can a cryogenic ion trap be designed to minimize the heat load on the cryostat? Another question that this trap might address in the near future is: what improvement in the ion reactive lifetime can be obtained by putting the trap in a cryogenic environment?	Designed and constructed a knife-edge ion trap system at 4K for strontium-88 ions with a cryogen hold time of one day.	4.1.1, 4.2, 4.3.2
What loading techniques can be used to reduce the heat load in a cryogenic trap, while providing quick and reliable loading? Can the amount of charge that accumulates on trap dielectrics while loading be reduced?	Loaded a trap in a cryogenic environment with strontium-88 ions using a novel laser ablation technique.	4.3.3
Can a residual gas pressure in a cryostat low enough to observe ion crystals be achieved, in a bath cryostat system with no vacuum pillbox?	Observed the transition of clouds into Wigner crystals and linear chains of ions in a knife-edge trap at 4K.	4.3.1, 5.3, 5.4
What is a good design for a cryogenic planar trap? What techniques can be used to load the trap in the presence of large stray fields expected in a planar trap? A question we hope to address in the near-term using this trap is: how much are heating rates in planar traps reduced by cooling them to 4K?	Designed a planar cryogenic trap for strontium-88 to be loaded using He buffer gas.	6.1, 6.2, 6.3, 4.1.2

1.5 Context and contributions

This work is part of a long-term project conducted by Prof. Isaac Chuang's group at MIT, in the Center for Ultracold Atoms, with the goal of investigating and understanding ion trap quantum information processing systems at a variety of scales. The group collaborates with Lucent Technologies that are currently in the process of developing silicon planar traps using lithographic fabrication. To give a sense of the scale of these traps, we note that the ion height above the silicon substrate is about

50μm. One goal of this work is to help prepare a way for trapping in Lucent's traps in a cryogenic environment.

I conducted the work described in this thesis in two stages, the first of which focused on planar trapping while second focused on cryogenic trapping. David Leibrandt constructed the macroscopic planar trapping system described in Chapter 2 based on an earlier version by Christopher Pearson. I took most of the data presented in that chapter: ion characterization, measurement of trap secular frequencies and geometric factors, and the quantitative characterization of ion movement operations. We published the results described in Chapter 2 in [PLB+06].

In the second stage, I collaborated with Christopher Pearson on testing the cryostat used in our experiments and milling the vacuum pillbox described in Chapter 4. I designed and built all parts of the cryogenic trap for strontium-88, except for the laser system which Kenneth Brown, Robert Clark and Jaroslaw Labaziewicz constructed earlier for testing their room temperature traps. I first loaded strontium-88 clouds using ablation into a home-made four-rod trap. For my later experiments, I used a trap provided by Prof. Urabe's group, our collaborators at Osaka University, to observe chains of resolved single ions. In collaboration with Paul Antohi, I designed and built the planar trap system described in Chapter 6, which we are currently trying to load with strontium-88 using He buffer gas.

Chapter 2

Macroscopic Planar Ion Trap Testbed

In preparation for trapping atoms in a planar trap, we investigate trapping macroscopic charged particles in printed circuit board (PCB) traps in a rough vacuum environment. We do not cool our ions, and imaging is accomplished by classical (off resonant) scattering of laser light. Because these experiments do not require an ultra high vacuum environment, we are able to achieve a fast cycle time for testing different electrode layouts. We optimize the electrode geometry to maximize the trap depth, and further demonstrate loading from a conventional four rod linear Paul trap acting as a reservoir of ions. Atomic ions could be laser cooled in the four rod trap before being transferred to the planar trap to circumvent the problem of low trap depth. We test trap layouts with segmented center electrodes and segmented outer electrodes, and demonstrate all three of the movement operations required for the Kielpinski et al. [KMW02] architecture. While transport, splitting and joining [R+02], and movement through intersections [H+05] have already been achieved in multi-level traps, this work represents the first realization of these operations in planar ion traps.

This chapter proceeds as follows. Section 2.1 offers a general discussion of planar ion trap design and a detailed description of our experimental setup. In Section 2.2, we characterize the macroscopic charged particles we use to test the traps. Section 2.3 presents the results of our investigation of planar ion traps including secular motion

and ion movement experiments. In Section 2.4 we discuss some of the various alternative trap geometries we have tested and propose a novel planar ion trap geometry that forms a lattice of point RF Paul traps. Finally, in Section 2.5 we summarize useful lessons learned that could be applied to atomic planar ion traps.

2.1 Experimental design

The design of a planar trap for trapping macroscopic particles involves three main considerations: the ion source, the ion loading scheme and the PCB design. Particle ion sources in common use include electrospray ionization [YF84], laser ablation [KBBH87, BCS89] and piezoelectric particle generation [AF86]. The careful choice of an ion loading mechanism is important because of the low trap depth of planar traps. The planar trap described in this paper is loaded using a four rod trap with a higher trap depth. Designing the PCB involves choosing the electrode dimensions to get the desired trap depth, ion height above the substrate and secular frequencies; choosing the layout of the control electrodes to allow for performing the desired movement operations; and choosing a PCB substrate that has a high voltage breakdown threshold, does not accumulate charge easily, and is vacuum compatible in the case of a trap in a UHV environment. This section begins by presenting some general considerations for planar trap design and proceeds to describe the experimental setup.

2.1.1 Trap design

The dynamics of an ion in a linear RF Paul trap are determined by solving the classical equations of motion. For an RF quadrupole electric potential

$$\phi(x, y, t) = \frac{x^2 - y^2}{2r_0^2} \left(U - V\cos(\Omega t)\right) \ , \tag{2.1}$$

the x and y equations of motion take the form of Mathieu equations:

$$\frac{d^2x}{d\tau^2} + (a - 2q\cos(2\tau))\, x = 0 \tag{2.2}$$

and

$$\frac{d^2y}{d\tau^2} - (a - 2q\cos(2\tau))\, y = 0\ . \tag{2.3}$$

Here $\tau = \Omega t/2$ is a dimensionless time, the Mathieu parameters $q = (2QV)/(mr_0^2\Omega^2)$ and $a = (4QU)/(mr_0^2\Omega^2)$ are dimensionless RF and DC voltages, and Q and m are the ion charge and mass. The motion is stable (i.e., the components of the ion position vector x and y are bounded in time) in regions of $a-q$ parameter space. In particular, for $a = 0$ the motion is stable for $0 < q \leq_{max}= 0.908$.

In the pseudopotential approximation, where $q \ll 1$, the ion motion along axis i can be decomposed into slow, large amplitude secular motion at the secular frequency ω_i and fast, small amplitude micromotion at the RF drive frequency Ω [Deh67]. For an electric potential of the form

$$\phi(x, y, z, t) = \phi_{RF}(x, y, z)\cos(\Omega t) + \phi_{DC}(x, y, z)\ , \tag{2.4}$$

the secular motion is determined by a secular potential

$$\psi_{sec}(x, y, z) = \frac{Q^2}{4m\Omega^2}|\nabla\phi_{RF}(x, y, z)|^2 + Q\phi_{DC}(x, y, z) \tag{2.5}$$

and for a particular set of initial conditions, the ion's motion in say, the x-direction, is given by

$$x(t) \approx A\cos\left(\beta\frac{\Omega}{2}t\right)\left[1 - \frac{q}{2}cos(\Omega t)\right], \tag{2.6}$$

where A depends on initial conditions and $\beta \approx \sqrt{a + q^2/2}$.

Using the secular potential we can calculate the height r_0 of the ion above the plane of the electrodes, the secular frequencies ω_i in the harmonic region of the potential, and the trap depth $\psi_{sec,0}$. The trap depth is defined in the usual way as the energy an ion would need to escape the trap. The secular potential for the planar trap used

in these experiments is shown in Figure 2-1.

In order to determine the optimum relative sizes of the trap electrodes, we have calculated the secular potential numerically for the planar trap geometry defined in Figure 2-1 over a range of dimensions using a two dimensional finite element electrostatic package named BELA [Mee04]. Here w_c is the width of the center electrode, w_r is the width of the RF electrodes, w_o is the width of the outer electrodes, g is the width of the gap between the center and the RF electrodes, g' is the width of the gap between the RF and outer electrodes, h is the height of a planar electrode which is parallel to the trap electrodes above the trap electrodes, r_0 is the height of the ion above the trap electrodes, and $r_1 = (w_c + w_r)/2 + g$ is a measure of the trap size. We set $g' = g$ and $w_o \to \infty$, and varied w_c, w_r, and h. Note that $h \to \infty$ for a true planar trap. Figures 2-2 and 2-3 show the normalized trap depth d_0 defined by

$$\psi_{sec,0} = \frac{Q^2V^2}{4mr_0^2\Omega^2}d_0 \ , \tag{2.7}$$

and the normalized secular frequency f_i defined by

$$\omega_i = \frac{QV}{\sqrt{2}mr_0^2\Omega}f_i \tag{2.8}$$

as functions of w_c/r_0 and w_r/r_0 for $h/r_1 = 706$. Note that $d_0 = f_i = 1$ for a perfect quadrupole trap and that we consider the secular frequency in the harmonic region of the potential where it is the same along both axes (this is appropriate when the ions are at low temperature).

Using Figures 2-2 and 2-3, we can design a planar trap to maximize the trap depth subject to the experimental constraints. As an example, consider a planar ion trap for $^{8}8Sr^{+}$. The ion height r_0 is set by either the acceptable ion heating rate or by how tightly the cooling and other lasers can be focused such that they do not scatter off the surface of the trap. Suppose we pick $r_0 = 500$ μm. The electrode widths w_c and w_r should be chosen to maximize the trap depth using Figure 2-2, subject to the constraint that the gap between them g must be large enough that the RF voltage does not induce electrical breakdown. In general, the optimum center

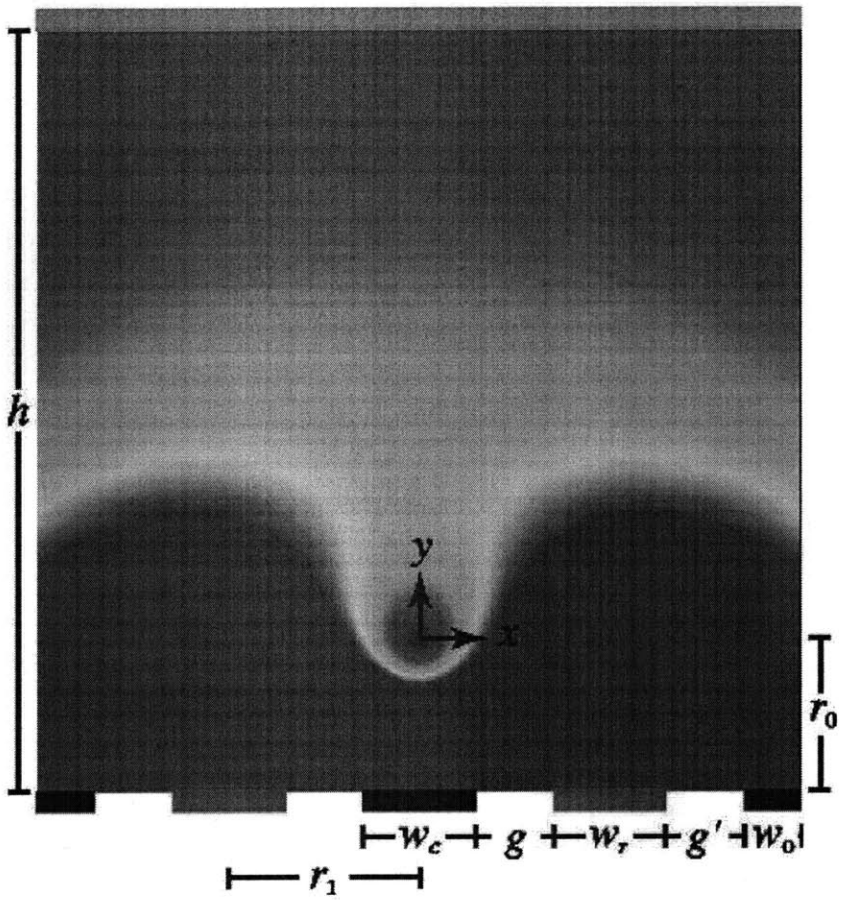

Figure 2-1: Secular potential for a planar ion trap. The particular geometry depicted is that of the cross trap described in Section 2.1.2. The secular potential is plotted on a linear color scale as a function of x and y, with blue representing the lowest and red representing the highest secular potential values. Secular potential values above twice the trap depth are truncated for clarity. The ion is located at the origin of the coordinate system. An RF potential $V\cos(\Omega t)$ is applied to the red electrodes, a DC potential U is applied to the blue top plate electrode, and the black electrodes are grounded.

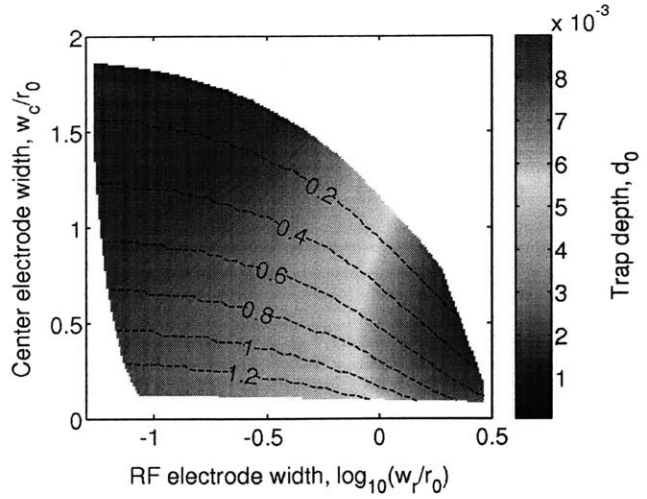

Figure 2-2: Trap depth versus electrode widths. The normalized trap depth d_0 is plotted in color as a function of $\log_{10}(w_r/r_0)$ and w_c/r_0 for $h/r_1 = 706$. The dashed lines are contours of constant g/r_0. Note that the maximum trap depth is obtained at $w_c/r_0 \approx 0.5$ and w_r/r_0 as large as possible.

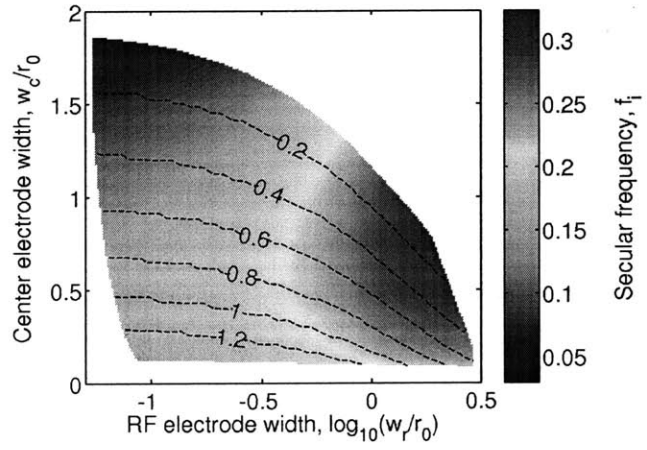

Figure 2-3: Secular frequency versus electrode widths. The secular frequency at zero ion temperature f_i is plotted in color as a function of $\log_{10}(w_r/r_0)$ and w_c/r_0 for $h/r_1 = 706$. The dashed lines are contours of constant g/r_0.

electrode width is around $0.5r_0$, and the optimum RF electrode width is as wide as possible given practical considerations such as the capacitance of a large electrode. For our example, suppose further that $g = 0.5r_0 = 250$ μm and $w_r = r_0 = 500$ μm. Figures 2-2 and 2-3, then, give $r_c = 0.58, r_0 = 290$ μm, $d_0 = 0.0065$, and $f_i = 0.28$. At $V = 500$ V and $\Omega = 2\pi \times 10$ MHz, this corresponds to $\psi_{sec,0} = 0.47$ eV and $\omega_i = 2\pi \times 1.1$ MHz.

We have found that by adding a planar top electrode (i.e., choosing h to be finite) biased at a positive DC potential U we can increase the trap depth by up to a factor of a 40 for a given RF amplitude and frequency. Figure 2-4 shows the normalized trap depth defined by

$$\psi_{sec,0} = \frac{Q^2V^2}{4mr_1^2\Omega^2}d_1 \ , \tag{2.9}$$

as a function of the normalized voltage on the top plate,

$$u = \frac{4mr_1^2\Omega^2}{QV^2}\frac{r_1}{h}U \ , \tag{2.10}$$

for $w_c/r_1 = w_r/r_1 = 0.6$ and several values of h/r_1. Note that the trap depth is normalized differently for this plot than it was for Figure 2-2. This is because r_0 is a logical starting point for selecting the electrode dimensions, but r_1 is the fixed length scale once the trap is built. At $u = 0$, the smallest barrier in the secular potential over which the ion can escape is in the positive y direction. As u increases, the minimum energy escape path shifts first to the sides and then to the negative y direction. For a given geometry, the trap depth increases with u until the minimum energy escape path is straight down to the center electrode, then decreases with a further increase in u. The maximum trap depth occurs at $u \approx 1$ and is given by $d_1 \approx 0.29$, or a little more than one fourth the trap depth of a standard four rod ion trap with similar dimensions. The secular potential depends only weakly on h/r_1 because the effect of nonzero u is well approximated by a constant electric field in the regime $h/r_1 \gg 1$ that we consider. Note that because the DC potential pushes the ion off of the RF quadrupole null, there will be increased micromotion. In practice we envision turning the DC potential on for loading, then gradually turning it off as the ions are laser

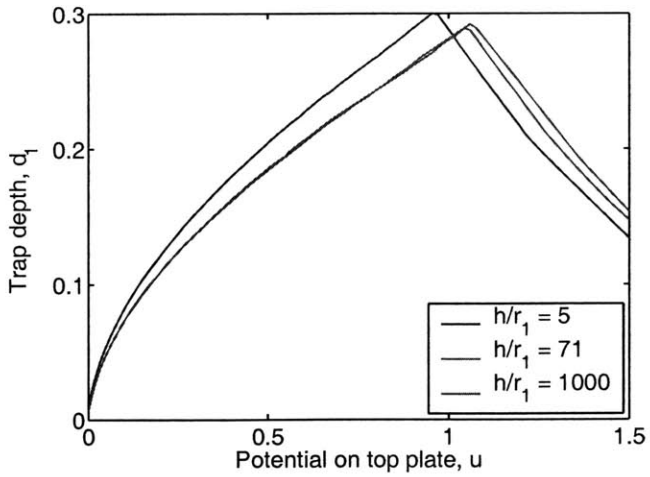

Figure 2-4: Trap depth versus top plate location and potential. The normalized trap depth d_1 is plotted as a function of u for $w_c/r_1 = w_r/r_1 = 0.6$ and several values of h/r_1. For $u \leq 0.2$, the ion escapes straight up in the positive y direction; for $0.2 \leq u \leq 1$, the ion escapes out to the side; and for $1 \leq u$ the ion escapes straight down in the negative y direction. Note that the maximum trap depth $d_1 \approx 0.29$ is obtained at $u \approx 1$.

cooled. Continuing our previous example, with a top plate electrode $h = 1$ cm above the trap biased at $U = 100$ V, we get a trap depth $\psi_{sec,0} = 4.6$ eV.

2.1.2 Experimental Apparatus

In this section, we discuss the specifics of the trap's design and construction, our source of ions, the method for loading the planar trap, the environment used for performing our experiments, and our methods for measurement and control of ions.

The planar trap we investigated is made up of four straight arms joined at a cross intersection (Figure 2-5). It is a printed circuit board (PCB), made using standard techniques. The electrodes are tin coated copper, and the substrate is GML-1000, a microwave laminate. The trap has a five electrode design, with outer electrodes segmented to control the axial potential. The center electrodes are also segmented at the intersection to provide additional control in that region. The center three electrodes are all 1.27mm wide, the electrode spacing is 0.89 mm, and the outer control electrodes are 2.5 mm long. We do not use the optimal electrode sizes as

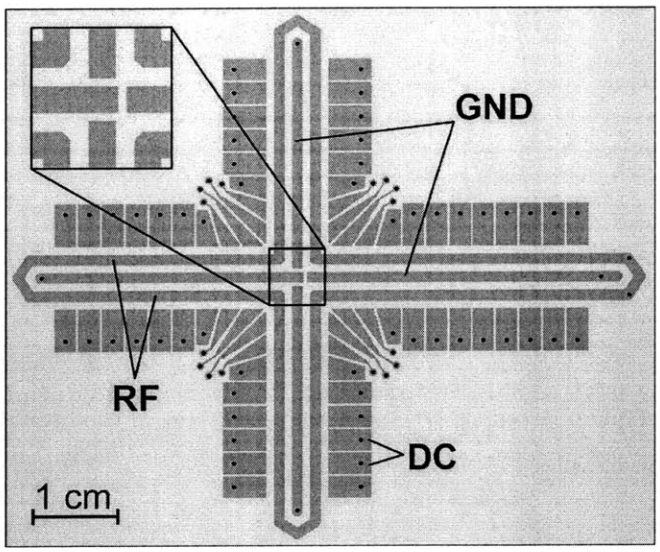

Figure 2-5: Top view of the trap. Opposing electrodes in straight sections of the trap are electrically connected, but near the intersection both the outer and center electrodes are separated to provide finer control. Electrical connections are made via surface mount headers on the underside. The RF loop at each end helps prevent ions from leaking out axially.

discussed in Section 2.1.1 due to the practical considerations of printed circuit board manufacture, specifically minimum feature and drill sizes.

Electrospray ionization (ESI) provides ions to the trap. This technique, commonly used with linear quadrupole filters for mass spectroscopy, applies high voltage to a liquid solution at a sharp tip. Strong electric fields at the tip blow off fine droplets of solution, and as solvent evaporates from these charged droplets, self-repulsion breaks them up into smaller particles, eventually producing individual charged solute particles. Following [CPK+02], we begin with a 5% suspension of 0.44 μm diameter aminopolystyrene spheres. We then prepare a solution buffered to pH = 3.9, add methanol to produce a 4:1 methanol/solution mixture, and add the spheres to produce a 0.05% suspension. The suspension is then placed in a sealed bottle, and pressurized to 50-100 kPa. This forces the liquid through a 0.45 μm filter to block any clusters of microspheres, and out the electrospray tip. The tip itself is made from fused silica capillary tubing, which is heated, stretched to produce a neck, and

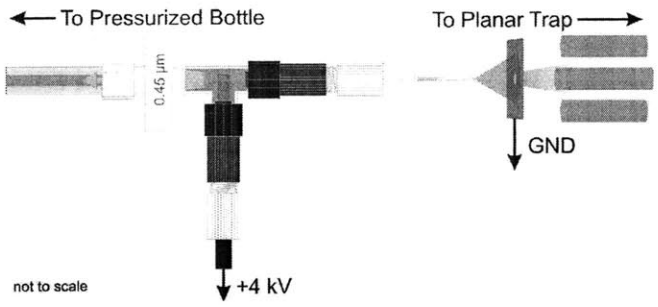

Figure 2-6: The ESI apparatus. Microspheres suspended in a mixture of methanol and water are forced from a pressurized bottle, through a 0.45μm filter and past a copper wire with +4 kV applied voltage, and out the capillary tip. This section is assembled from standard luer fittings. The charged spray passes through a mask and into a four rod trap.

cleaved to produce a 100 μm opening. We apply 4 kV directly to the liquid with a copper wire inserted in the fluid near the tip (Figure 2-6). The spray plume from the tip is directed through a grounded mask and into the end of a four rod trap.

By arranging the rods so that they match the strips of a planar trap, we interface the four rod trap directly to the planar trap. A slot cut in the side of the PCB allows us to lower the four rod trap to a point where its trap axis coincides with that of the planar trap (Figure 2-7). Mutual repulsion of ions loaded in the far end of the four-rod trap forces them along, eventually pushing them into the planar trap. When completely full, the planar trap can hold $\sim$50 ions.

Electrospray ionization must be performed at or near atmospheric pressure, and experiments on free trapped particles require a vacuum, so we enclose both four rod and planar traps in a custom built clear acrylic box (Figure 2-8), and load through an open side of the box. We perform all loading at atmospheric pressure, then seal the box shut and carefully pump down. We use a needle valve to control flow rate during pumping, since any significant air flow can push ions out of the trap. The lowest attainable pressure in this enclosure is about 15 Pa (10^{-1} torr). Green (532 nm) laser light directed along the trap axes illuminates ions by classical (off resonant) scattering. The ions are clearly visible by eye, and we photograph them using an ordinary camera lens mounted on a CCD camera.

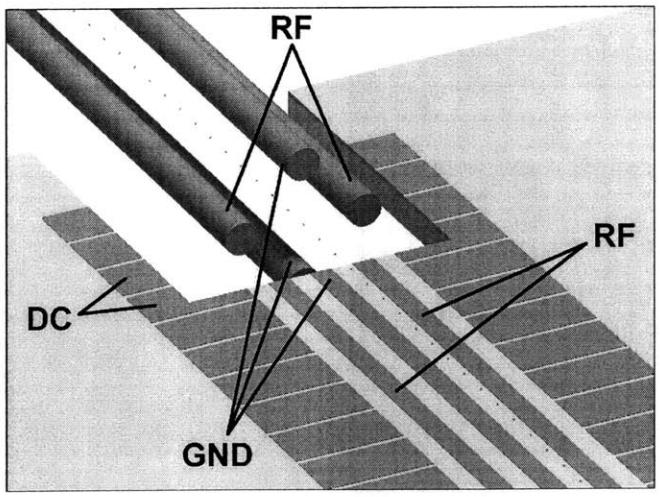

Figure 2-7: Four rod to planar interface. A slot cut in the planar trap allows for a common trap axis. The large particles form a linear Wigner crystal immediately and are pushed into the planar trap.

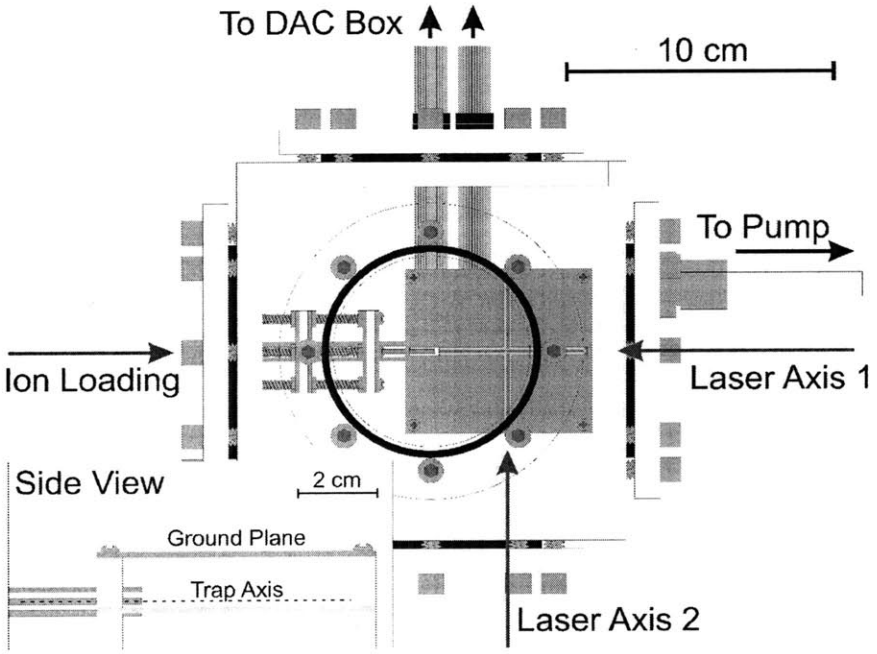

Figure 2-8: Top view of the vacuum chamber. Ions are loaded into the left side, and then a flange is screwed into place and the air evacuated slowly. Two green lasers illuminate the trap axes.

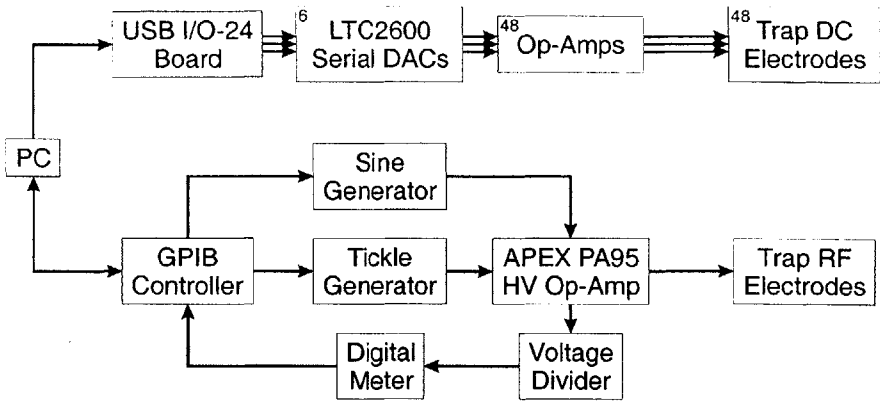

Figure 2-9: Control electronics for the planar trap.

Also shown in Figure 2-8 is a metal plate installed above the trap to increase its trap depth and shield from stray static charge. Machined slots in this plate allow us to view ions from above, but we can also see them from the side. This slotted top plate design has the advantage of masking laser scatter, but for more complex trap topologies it might be easier to use a transparent conductor such as indium tin oxide or a thin film of gold [Gor00, GH02, SHKS01]. This could be deposited on a glass plate or directly on the vacuum window or an imaging optic inside the vacuum chamber.

The electronics used to generate the RF and DC potentials for the trap are shown in Figure 2-9. Frequencies for which the microspheres are stable range from a few hundred hertz to several kilohertz, depending on the pressure. This is in the audio frequency (AF) range, but we will continue to refer to it as RF. Since these frequencies are easily synthesized, we use a function generator as the source, then use an active high voltage amplifier to reach the target voltage range. A small tickle signal can be added to the main RF signal before amplification to probe for resonances in ion motion, allowing us to determine secular frequencies (Section 2.3.2). In this design, the upper limit to RF voltage is set by arcing between RF and ground electrodes, which occurs at about 400 V amplitude. Typical operating conditions are about 250 V and 1.5 kHz.

To provide DC control of the trap's 48 independent electrodes, we use a board

with 24 digital output channels to address six serial octal digital to analog converter (DAC) integrated circuits. The outputs of these DAC chips are then amplified to ± 20 V, sufficient to axially confine or to move these particles.

2.2 Ion characterization

Our goal in this work is to study the properties of planar traps rather than the ions loaded into them. To be able to draw conclusions about atomic ion traps from work on macroscopic ions, we must (i) scale away the charge-to-mass dependence from measured parameters and (ii) understand the effect of damping on macroscopic ions since it is almost negligible for atomic ions. Section 2.2.1 discusses measurement of the Q/m spectrum of the ions. Section 2.2.2 discusses the effects of air drag on the ions' stability and motion.

2.2.1 Charge to mass ratio

The principal drawback of using macroscopic charged particles to investigate a trap design is that, unlike atomic ions, these particles are not identical. Electrospray ionization (ESI) is a soft ionization technique that produces multiply charged ions with a significant spread in the charge state. The variation in the mass of the microspheres ($\approx 10\%$) also contributes to broadening the charge-to-mass distribution. Nevertheless, we are able to keep the Q/m spectrum constant by maintaining constant electrospray pressure, voltage, capillary diameter and loading parameters.

To measure the Q/m spectrum of the ions, groups of about five ions at a time were loaded into the four rod trap with $\Omega = 2\pi \times 2$ kHz and $V = 250$ V. With the chamber pressure at 70 Pa, the RF frequency was lowered while observing the ejection frequency Ω_{ej} of each ion. The charge-to-mass ratio was calculated using the formula $Q/m = q_{max} r_0^2 \Omega_{ej}^2/(2V)$, where $q_{max} = 0.908$, the value of the Mathieu q parameter at the boundary of the first stability region of a quadrupole trap. Figure 2-10(a) shows a spectrum obtained for 178 ions with mean $Q/m = 1.17 \times 10^{-8} e$/amu (electronic charges per nucleon mass).

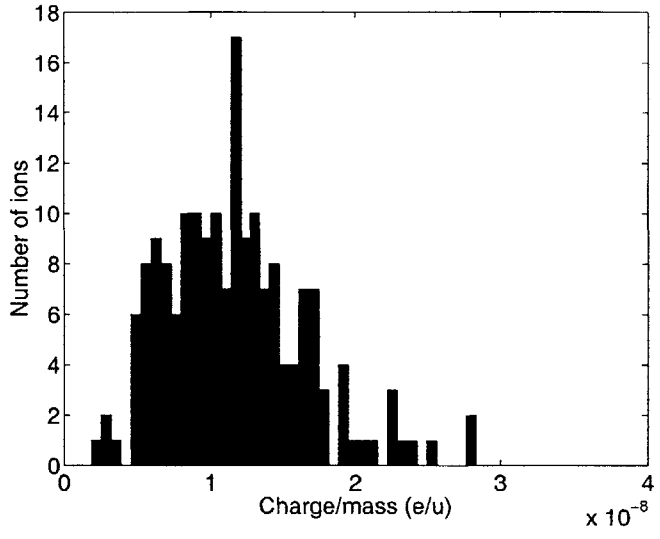

[t]

Figure 2-10: Charge-to-mass distributions of ESI-generated ions. The mean Q/m is 1.17×10^{-8} e/amu and the standard deviation is 0.49×10^{-8} e/amu.

2.2.2 Damping of ion motion by background gas

When trapping macroscopic ions at atmospheric pressure or in rough vacuum, the background gas exerts a drag force on the ions that both stabilizes the radial motion and slows down the axial ion movement operations. It is important to verify that the background pressure in our experiments is low enough to make accurate assessments of the trap performance.

For small Reynolds number $N_{Re} = 2\rho\dot{x}R/\mu$ and small Knudsen number $N_{Kn} = \lambda/R$, the drag on a sphere is given by Stokes' law

$$F_D = -6\pi\mu R\dot{x} \ . \tag{2.11}$$

Here ρ is the density of the gas, R is the radius of the sphere, μ is the dynamic viscosity, λ is the mean free path, and $\dot{x}$ is the ion velocity along the x axis. When the Knudsen number is large, Stokes' law overestimates the drag because the flow is no longer continuous. We divide Equation (2.11) by an empirical slip correction factor

$$C(N_{Kn}) = 1 + N_{Kn}\left(1.165 + 0.483e^{-0.997/N_{Kn}}\right) \tag{2.12}$$

to obtain an expression for the drag force which is valid at large Knudsen number [KMKP05].

We determine the effect of drag on stability by considering a modified dimensionless equation of motion

$$\frac{d^2x}{d\tau^2} + b\frac{dx}{d\tau} + (a - 2q\cos(2\tau))\,x = 0 \tag{2.13}$$

where the dimensionless drag coefficient

$$b = \frac{12\pi\eta R}{C(N_{Kn})m\Omega}. \tag{2.14}$$

A similar equation holds for the y motion. For $b = 0$, this reduces to Equation (2.2). Numerical computations verify that the region of stable trapping in $a - q$ parameter space grows with increasing b [WO91, NF01]. In particular, the maximum stable Mathieu q parameter at $a = 0$ goes from $q_{max} = 0.908$ at $b = 0$ to $q_{max} = 1.05$ at $b = 0.45$. The drag parameter b is plotted as a function of vacuum pressure p in Figure 2-11. At 40 mPa (0.5 torr), $b = 0.45$ is already less than 1 so air drag has only a small effect on the trap stability in these experiments.

The speed of ion motion in our shuttling experiments, however, is significantly affected by drag. The physical reason for this is that the characteristic time for shuttling experiments is much longer than the characteristic time for stability ($1/\Omega$). As a simple model, consider an ion which starts from rest at $z = 0$ in an axial potential

$$\phi(z) = \begin{cases} E(d - z) & , \quad z < d \\ 0 & , \quad z > d \end{cases} \tag{2.15}$$

and suppose we measure the ion velocity when $z = d$. In this model the length scale d is of the order of the axial dimension of a control electrode, and the electric field E is of the order of the electric potential applied to a control electrode divided by its axial dimension. Drag is important when the dimensionless drag parameter $c = \gamma t_d \geq 1$ where $\gamma = -F_D/(m\dot{z})$ and t_d is the time to reach $z = d$. Here t_d is the solution to

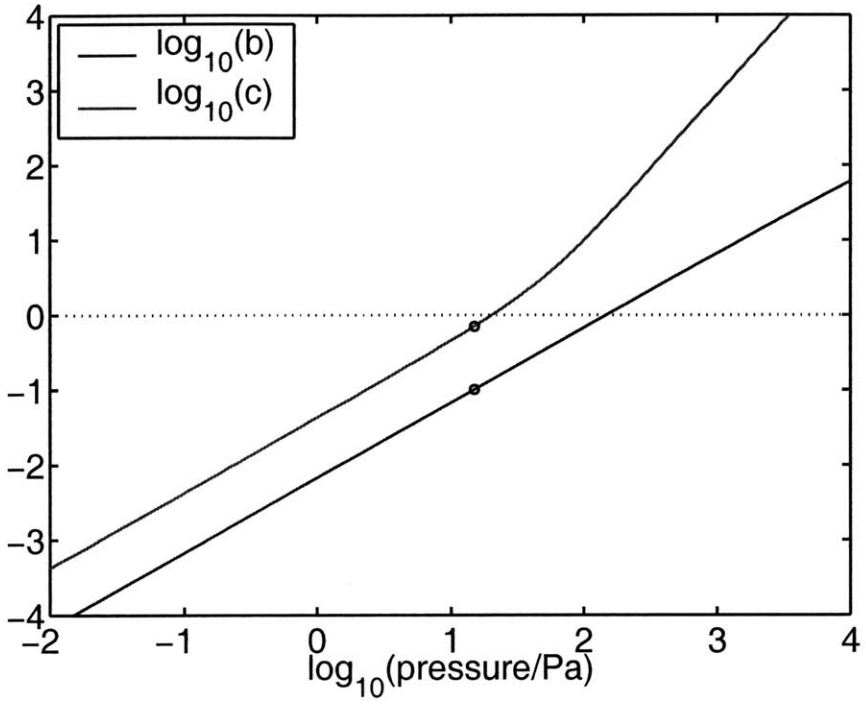

Figure 2-11: Drag coefficients describing ion stability and the speed of linear ion shuttling versus background pressure. The dimensionless drag coefficients b and c for stability and ion shuttling, respectively, are plotted as functions of the vacuum chamber pressure on a log-log scale. The drag coefficients are computed using $R = 0.22$ μm, $Q = 5.3 \times 10^{-17}$ C, $m = 4.7 \times 10^{-17}$ kg, $\mu = 1.83 \times 10^{-5}$ kg m^{-1} s^{-1}, $\lambda = (67.3 \text{ nm})(10^5 \text{ Pa}/p)$, $\Omega = 2\pi \times 5$ kHz, $d = 1$ mm, and $E = (1 \text{ V})/(1 \text{ mm})$; which is appropriate for the cross trap assuming that we are trapping single microspheres. The circles indicate the values of the drag coefficients at the pressure used in our experiment.

the transcendental equation

$$d = \frac{QE}{\gamma m}\left(t_d + \frac{e^{-\gamma t_d} - 1}{\gamma}\right) . \tag{2.16}$$

The dimensionless drag coefficient c is plotted as a function of pressure in Figure 2-11. At 40 mPa, $c = 4.9$ so drag plays an important role in ion shuttling experiments in the cross trap despite the fact that the trap stability is not affected by damping.

For large damping ($c \gg 1$), $\dot{z}(z = d)$ approaches the terminal velocity $(QE)/(\gamma m)$. The drag coefficient $\gamma \sim 1/C(N_{Kn}) \sim 1/N_{Kn} \sim p$, so $\dot{z}(z = d) \sim 1/p$. This is experimentally verified in Section 2.3.3.

2.3 Planar trap performance

When damping forces can be neglected, the Mathieu equations of motion of a trapped ion depend only on dimensionless parameters. It follows that the dynamics of macroscopic charged particles, viewed in the appropriate time scale (a micromotion period), are identical to that of atomic ions, and can be fully explored without the much more demanding experimental requirements of trapping atomic ions [HB93]. We have found macroscopic charged particle planar traps to be a rapid and accurate test bed for investigating traps of different geometries (e.g. three electrode, five electrode) and control electrode layouts (e.g. segmented center, segmented outer electrodes). In this section, we present the results of an experimental investigation of planar trap performance using this test bed.

2.3.1 Ion height above trap substrate

A planar trap with a segmented center electrode can be used to control the height of individual ions above the substrate by applying DC voltages to the electrode segments. One advantage of such control in a quantum computer is the ability to perform single qubit gates on different ions using a single stationary laser beam. The laser beam would have to be parallel to the ion chain but slightly raised or lowered. By changing

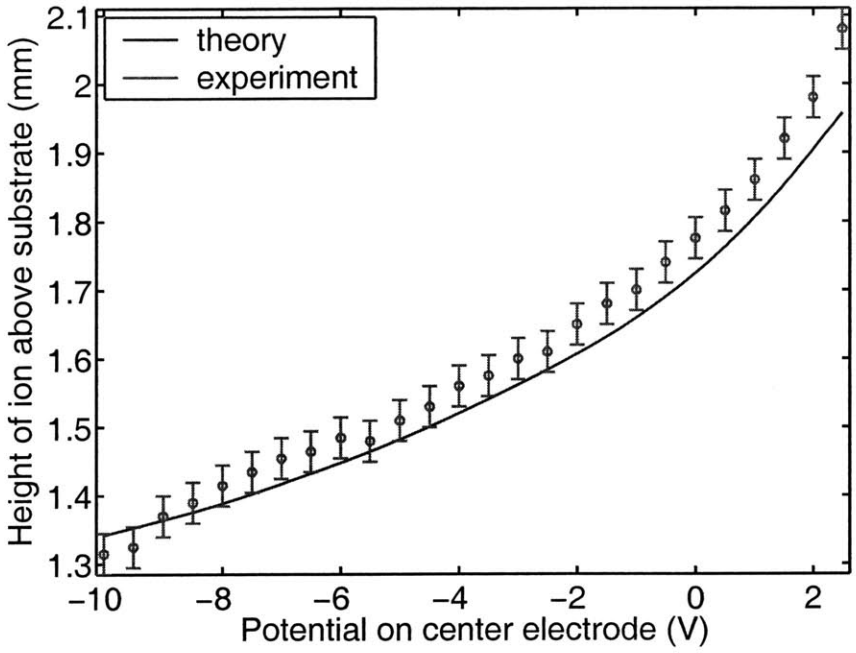

Figure 2-12: Ion height above the trap substrate, r_0, is plotted as a function of the DC potential on the center electrode. The solid line is the expected ion height from numerical computations of the secular potential as described in Section 2.1.1 using the measured charge-to-mass ratio of the ion.

the height of individual ions, they can be brought into the path of the beam to perform single qubit gates.

We measured the height of an ion above the trap substrate using a CCD camera mounted on a calibrated translation stage. The micromotion of the ion in the y direction causes the images (which have an exposure time much longer than the period of the RF drive) to show a streak where the ion is located, so we actually measured the positions of the top and bottom of the ion motion. Figure 2-12 shows the average of the positions of the top and bottom of the ion motion as a function of the DC potential on the center electrode. We measured Q/m for the ion by lowering the RF drive frequency until the ion becomes unstable as described in Section 2.2.1. The expected ion height shown in Figure 2-12 is calculated using this value of Q/m and a numerical computation of the secular potential.

Figure 2-13 shows the amplitude of the micromotion as a function of the DC

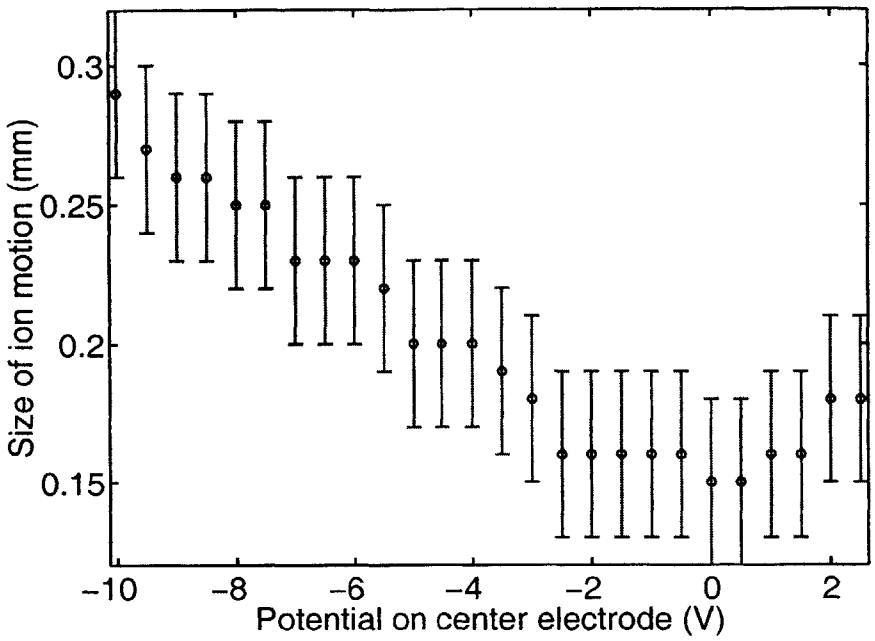

Figure 2-13: Micromotion amplitude. The peak to peak amplitude of the micromotion in the y direction is plotted as a function of the DC potential on the center electrode.

potential on the center electrode. The micromotion is minimized when the ion is located at the null of the RF quadrupole electric field as expected, which occurs when the potential on the center electrode is zero.

2.3.2 Secular frequencies and trap geometric factors

We determine the secular frequency of an ion by adding a Fourier component of frequency Ω_t and amplitude V_t to the RF signal. Typically, V_t is between 0.5 V and 2 V. By sweeping Ω_t, we are able to observe a sharp increase in the size of the ion trajectory along the direction of the secular mode excited by the drive signal as seen in Figure 2-14. Although the drive signal is applied to the RF rods, indirect coupling of the drive to the axial motion of the ion is sufficient to excite axial modes. The exact axial secular frequency depends on which trap electrodes are used as endcaps and what voltage is applied to them, but it is typically between 15 Hz and 30 Hz. The transverse secular frequencies are of more interest because they depend directly

[h]

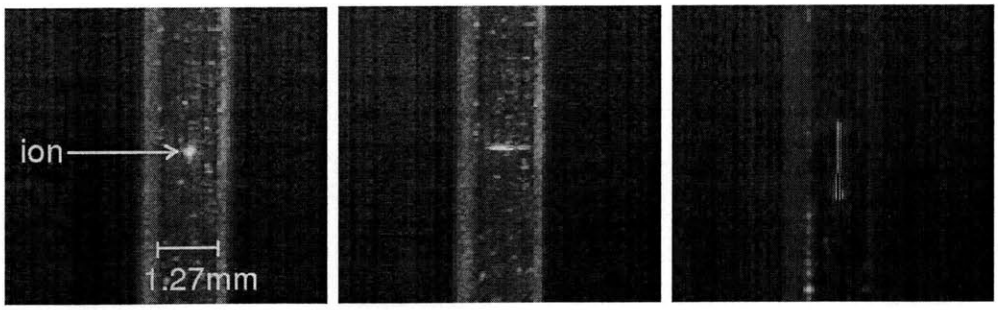

(a) (b) (c)

Figure 2-14: (a) Top view of an ion trajectory from secular resonances with $V = 250$ V and $\Omega = 2\pi \times 2$ kHz. Only the center ground electrode is seen in these pictures because the grounded top plate electrode masks the other electrodes from view. The width of the ground electrode is 1.27 mm. (b) Transverse mode excited at a drive frequency of 288 Hz. (c) Axial mode excited at 25 Hz.

on the trap geometry: the geometric factor f_i/r_0^2 in Equation (2.8) depends only on electrode dimensions and their spacing. We were not able to resolve separate resonant frequencies for ω_x and ω_y, which indicates that the ion energy is much less than the trap depth. Figure 2-15 shows the dependence of the x secular frequency on V and Ω. Both dependences behave as expected from the pseudopotential approximation.

To confirm the accuracy of our simulations of pseudopotentials in planar traps, we measured the ratio of the geometric factor f_x/r_0^2 in the planar trap to that of the loading four rod trap. The large spread in the Q/m distribution does not allow for the determination of the geometric factor for each trap separately. However, we can measure the ratio of the geometric factors of the traps by first measuring ω_x of an ion in the planar trap, then applying a sequence of voltages on the control electrodes to move that ion into the four rod trap, where ω_x is measured again. By doing several experiments of this kind, we determined the geometric factor ratio to be 0.40 ± 0.01. Numerical simulations of this setup were also performed using BELA, giving for this ratio the value 0.404, which is within the error bar of the experimental result.

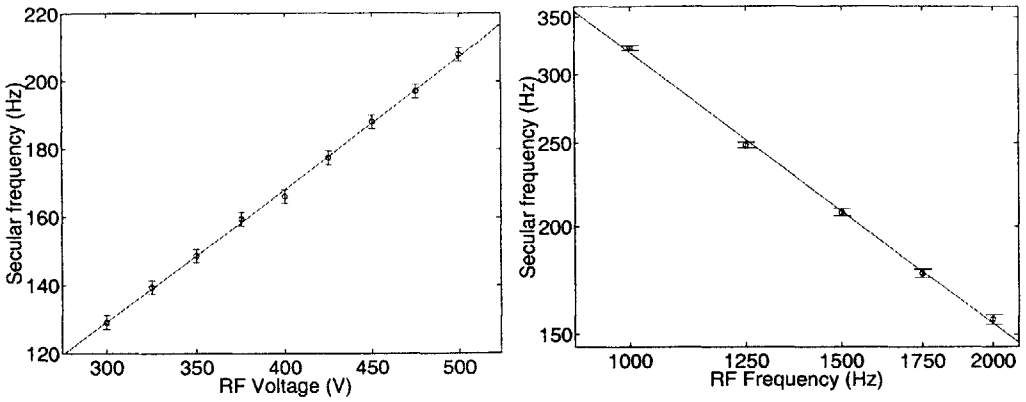

[h]

Figure 2-15: Measurements of the secular frequency versus (a) RF amplitude at fixed a fixed RF frequency of 1.5 kHz (on a linear scale) and (b) RF frequency at a fixed RF amplitude of 250 V (on a log-log scale). The solid lines are fits to Equation 2.8 with $\frac{Q}{m} f_i$ as a fit parameter.

2.3.3 Ion movement

Three important ion movement primitives for a multiplexed ion trap quantum computer are shuttling, turning corners and splitting/joining two ions [KMW02]. We have demonstrated these three operations in planar traps, using our macroscopic charged particle system.

We have also shuttled ions using another scheme where the nearest control electrodes on both sides of an ion are used to create a confining well along the axial direction. By moving this well along the trap, we had more control over the acceleration, speed and final position of the ion.

Splitting a pair of ions was performed by using the control electrodes to introduce a potential hill that pushes the ions apart. The ion spacing is approximately equal to the axial dimension of one control electrode, so this technique is satisfactory. Typically, an electrode between the ions is raised to 5 V for separation and lowered back to 0 V to join them again. For performing two qubit gates with atomic ions, it is desirable to bring the ions as close to each other as possible, because gates are fastest when the frequencies of the two axial normal modes of the ions are well separated [SS03]. In that case, the ion spacing is likely to be smaller than the electrode spacing, and

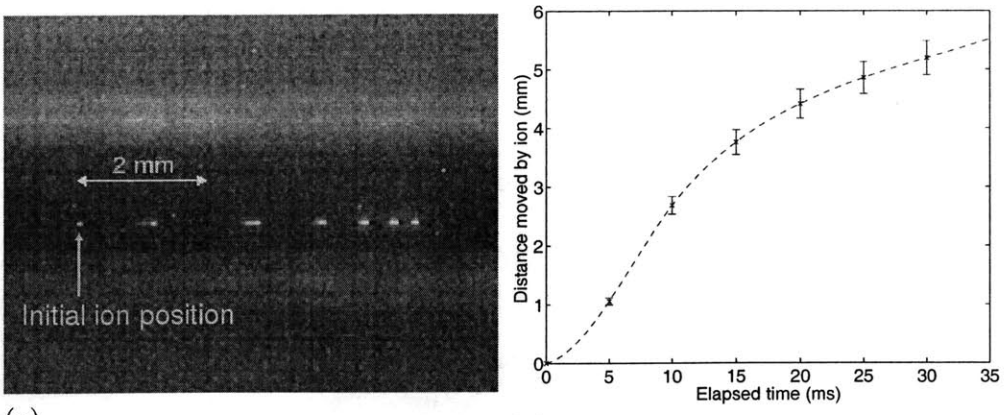

(a) (b)

Figure 2-16: (a) A strobe image showing shuttling of a single ion, taken by modulating the current to the illuminating laser. The laser is periodically turned on for 2 ms and off for 5 ms. The ion is moving from left to right; there is a short acceleration period after which the ion reaches a maximal velocity and then decelerates. This shuttle was performed by applying a potential of 5 V to the nearest control electrode that is to the left of the ion. (b) Distance moved by the ion vs. elapsed time, fitted with a spline to guide the eye.

it has been shown that it is advantageous to use the DC electrodes to produce an electric octopole moment for fast separation [HS03].

Figure 2-18 shows an ion turning a corner in the planar trap. Simulations of the pseudopotential indicate that there are potential hills in the RF nodal lines in each of the four arms close to the intersection, with a point node right at the intersection. To turn a corner, it is necessary for an ion to overcome the hills in both the source and destination arms. We have used the following pulse sequence to do that: (1) lower the center ground electrode of the destination arm to -2 V, then (2) raise a control electrode in the source arm to 5 V to push the ion over the hill in the source arm. We find that the ion has enough kinetic energy after traversing the first potential barrier to also overcome the second one.

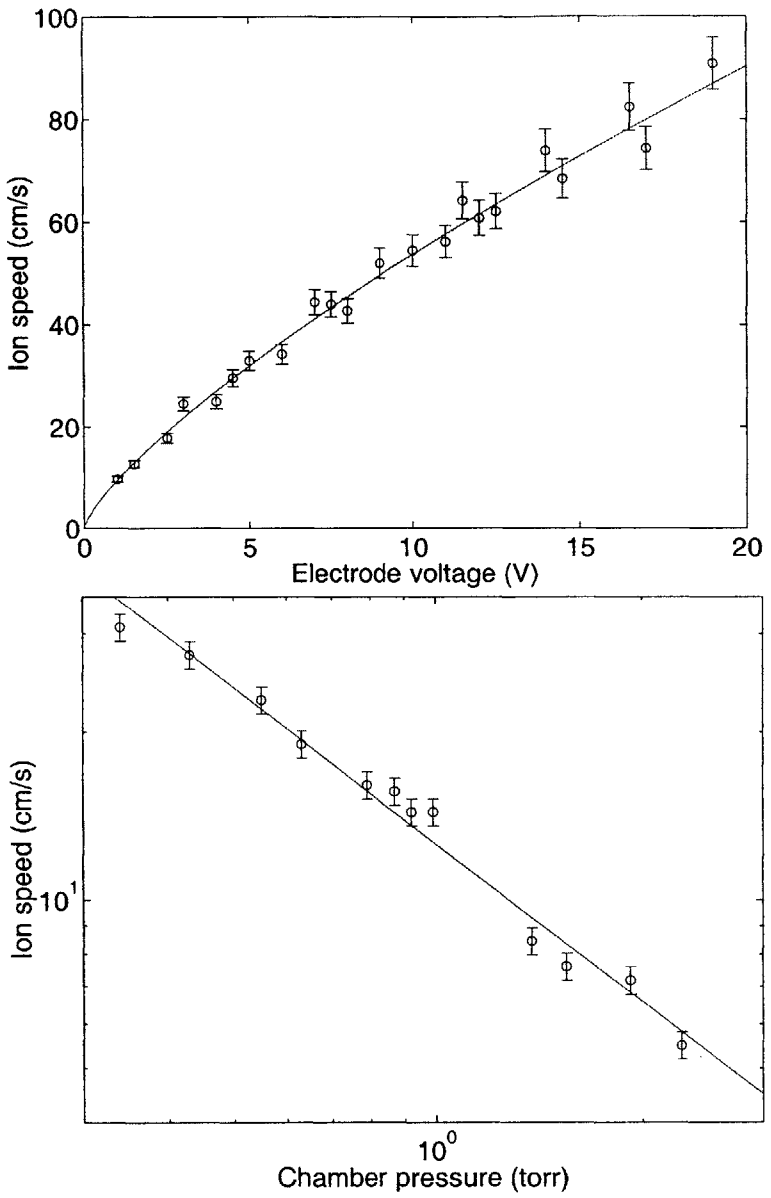

Figure 2-17: The maximum speed v_{max} an ion attains during a shuttling operation versus (a) the potential u_c applied to the nearest control electrode at constant pressure (40 Pa) fit to a 3/4 power law ($v_{max} = Au_c^{3/4}$ where $A = 9.55$ cm $s^{-1}V^{-\frac{3}{4}}$) (b) the chamber pressure at constant control electrode voltage (5 V). Ion speed is found to be inversely proportional to the chamber pressure. This behavior is expected when (1) the mean free path is much greater than the radius of the particles and (2) $\gamma t_{ac} \gg 1$ where γ the damping factor and t_{ac} is the acceleration time of the ion. When the damping is low enough such that (2) no longer holds, the ion speed is expected to reach a pressure-independent value.

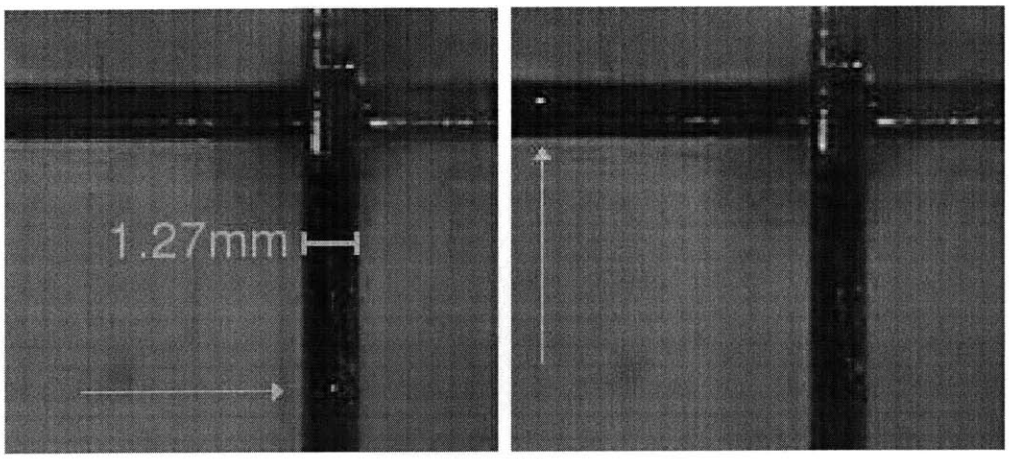

(a) (b)

Figure 2-18: Turning a corner. The arrows point to the position of the ion (a) before and (b) after turning the corner. This operation takes about 50 ms.

2.4 Variations on trap design

Macroscopic charged particles and PCB traps allow us to rapidly test a variety of planar trap layouts. We have focused on the loading and transport properties of multi-zone linear traps that are joined at intersections. In addition to the cross trap described in this paper, designs under investigation have as many as 100 zones and include corners, three way junctions, and four way junctions. These elements are necessary to generate the ion trap geometries that arise in complex quantum computation geometries [KMW02], particularly those involved in realizing scalable, fault-tolerant quantum computation circuits [SCA+04].

In addition to fault-tolerant quantum computation, ion traps are promising candidates for quantum simulations. Porras and Cirac have proposed using the motional modes of coupled ions to simulate Bose-Hubbard models [PC04]. The planar version of a point Paul trap is a natural way to implement this scheme for a two dimensional system. Starting with a plane of RF voltage one can place DC electrodes at arbitrary positions defining a planar point trap at each position. The distance between trapping points controls the strength of vibrational coupling and the layout of the electrodes can be used to create both ordered and disordered systems.

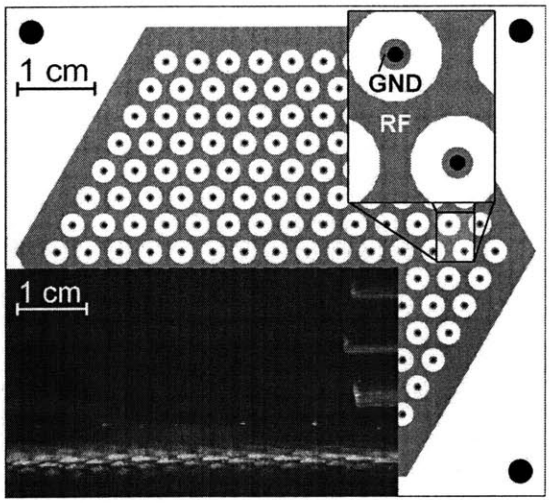

Figure 2-19: Top view of a two dimensional Paul trap array. Ions can either be confined to points or free to move along lines, depending on the RF and ground connections. The connections shown (top inset) trap ions above the dots. Bottom inset: Microspheres are trapped in the 2D array, and seven are shown illuminated by the laser beam. In contrast with the cross trap, the four rod loading stage is out-of-plane, and is visible above and to the right.

Using this approach, we have implemented a hexagonal lattice of traps shown in Figure 2-19; this lattice successfully trapped macroscopic ions. For experiments with single atom ions, the lattice spacing needs to be $\sim$50 μm to be near interesting phase transitions in condensed matter systems such as that studied by Porras and Cirac. Such a trap can be operated as described above with the ions trapped at the lattice points as shown in Figure 2-19. If the RF and ground electrodes are switched, the ions are trapped along the honeycomb lines, and applying an offset voltage to the RF on the dots moves the ions through the lattice. This increased coordination between ion positions may improve fault-tolerant thresholds.

2.5 Conclusions

We have experimentally demonstrated the planar ion trap design using macroscopic charged particles as a rapid development test bed. We have addressed the challenges of ion loading and ion motion given the smaller relative trap depth of planar traps.

The challenge of loading ions into the planar trap was solved by coupling a traditional four rod trap to a planar trap. Ions at high kinetic energy were first loaded into the linear trap and then offloaded onto the planar trap. This method allows us to load the planar trap with the efficiency of loading a traditional linear trap.

Furthermore, we have found that the addition of a charged conductive plane above the trap can be used to increase the trap depth. In the atomic case the ions will be initally loaded at a position of high micromotion limiting the effect of laser cooling. In our design example this micromotion has an amplitude of $0.04r_0$ when the potential on the top plane is such that the trap depth is increased by a factor of 10. However, after initial trapping the micromotion can be minimized and the cooling maximized simply by grounding the conductive plane.

Controlled movement of the ions in the planar trap was accomplished despite the small trap depth. Using increasingly complex traps, we have been able to perform all the fundamental movement operations required in a multi-zone architecture: splitting and joining ion chains and moving ions around corners and through four way intersections. Before this work, ion movement through a four way intersection was predicted to not be possible.

Questions remain about the control of ions at low vacuum. Our experiments were performed at a vacuum where the background pressure no longer effects trap stability. However, the pressure still contributed a significant drag term to the linear motion.

Additionally, we have demonstrated that planar traps can be used to produce a wide range of geometries. As an example, we have trapped in a hexagonal lattice. A similar trap for atomic ions could be used to simulate two dimensional quantum simulations. One can then controllably introduce disorder into the system by application of voltages or changes in trap fabrication.

Chapter 3

The Strontium Ion and its Lasers

The initial phase of my thesis work was trapping macroscopic ions, as described in the previous chapter. The remainder of my thesis work focused on trapping atomic ions, both in planar traps, and in a cryogenic environment, as described in this and the following chapters.

The list of candidate atomic ions for quantum computation is rather short; the singly-ionized species should preferrably be hydrogenic, which restricts our choices to Group II elements and a few other transition metals. The ion we use is $^{88}Sr^{+}$, and its choice is largely motivated by the fact that its Doppler cooling transition can be driven using a diode laser. Diode lasers can be cheap and easily tunable, which makes them an attractive option over deep UV lasers required for most other ions.

The outline of this chapter is as follows. In Section 3.1, we give an overview of the energy level structure of $^{88}Sr^{+}$ and the characteristics of the transitions used in our experiment. In Section 3.2, we describe the design and operation of the lasers that drive these transitions.

3.1 The strontium ion

Strontium-88 is the most common isotope of strontium (natural abundance 82.6%). It has no nuclear spin, and thus no hyperfine structure. Figure 3-1 shows the energy level diagram of the ion and the spontaneous emission lifetimes for the various transitions.

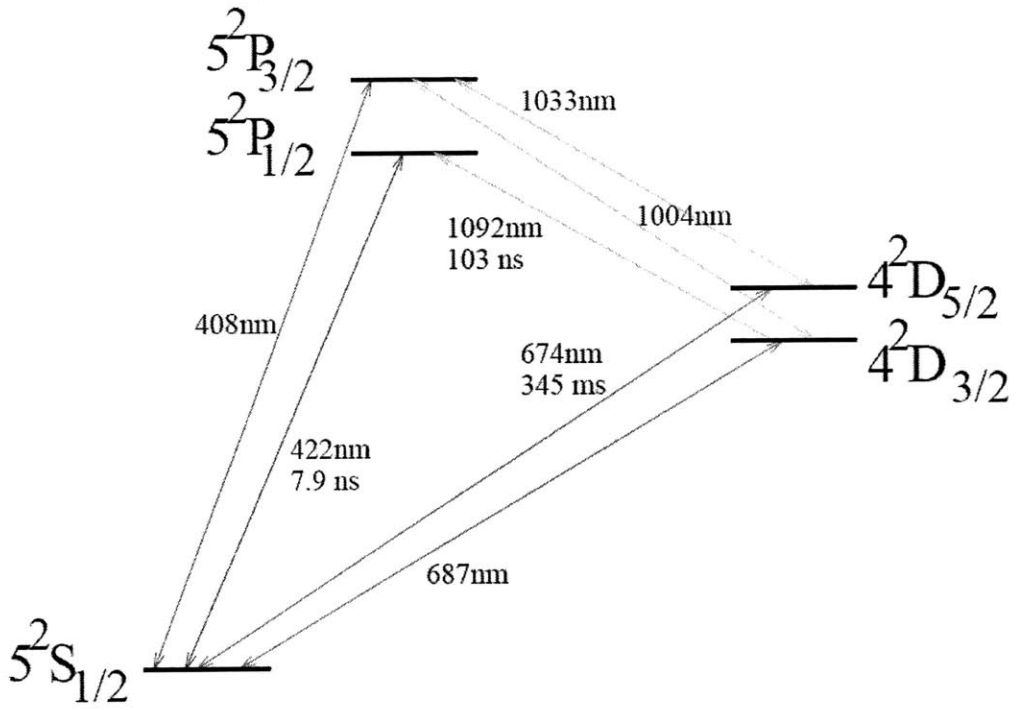

Figure 3-1: Energy level diagram of $^{88}Sr^+$. The exact wavelengths in vacuum of the blue and IR transitions used in this experiment are 421.671nm and 1091.787nm.

The transitions of interest are:

1. $5^2S_{1/2} \leftrightarrow 5^2P_{1/2}$ 422nm transition: this is a strongly dipole-allowed transition that is used for imaging the ions via resonant scattering and for Doppler cooling. The width of the transition is 22MHz, which sets a limit on the temperature that can be achieved via Doppler cooling of $T = \hbar\Gamma/2k_B = 84\mu$K.

2. $5^2P_{1/2} \leftrightarrow 4^2D_{3/2}$ 1092nm transition: one in 14 decays from the $5^2P_{1/2}$ state is to the $4^2D_{3/2}$ state [Ber02], which makes a repump laser at this wavelength necessary to avoid depopulation of the principal transition.

3. $5^2S_{1/2} \leftrightarrow 4^2D_{5/2}$ 674nm transition: this dipole-forbidden transition has a lifetime of 345ms and its frequency has been measured to 3.4 parts in 10^{15}, making it one of the most accurate optical frequency standard in the world [KBG+03]. It would eventually serve as a good optical qubit because of its long lifetime.

It can be used for measuring the temperature of trapped ions since it is not a cooling transition. The temperature of the ions is extracted from the ratio of the zero-detuning and sideband peaks in a spectrum obtained by sweeping the frequency of this laser [DBIW89]. Finally, this transition can be used for resolved sideband cooling of the ion to the motional ground state.

4. $4^2D_{5/2} \leftrightarrow 5^2P_{3/2}$ 1033nm transition: a quencher laser addressing this transition would be required to speed up the sideband cooling process by mixing the $4^2D_{5/2}$ state with the much shorter lived $5^2P_{3/2}$.

Of the transitions above, only the first two are used in the experiments described in this work.

3.2 The blue and IR lasers

We use diode lasers because they are small, inexpensive and easily tunable. A diode laser is a p-n junction formed by two semiconductor layers. When an injection current is applied through the junction, carrier recombination in the depletion layer produces incoherent light. Above a certain current threshold, photons moving parallel to the junction stimulate emission and initiate laser action with the p-n junction itself acting as a cavity [Pan76, Tho80]. Linewidths are typically 10 to 100MHz but can be reduced to about 1MHz by using an external cavity diode laser apparatus (ECDL) [Cam85, Tho05].

Figure 3-2 is a schematic of the blue (422nm) laser apparatus. An external cavity is formed between the p-n junction and a diffraction grating outside the laser. The first order diffraction is sent back to the laser for feedback and the zeroth order is the output. The lasing wavelength can be finely adjusted by adjusting the position of the grating using a piezo-electric device, which we refer to as the "grating piezo".

Most of the ECDL output of the blue laser goes to the ion trap; a small fraction of it is used for measurement of the frequency and its stabilization, as described below.

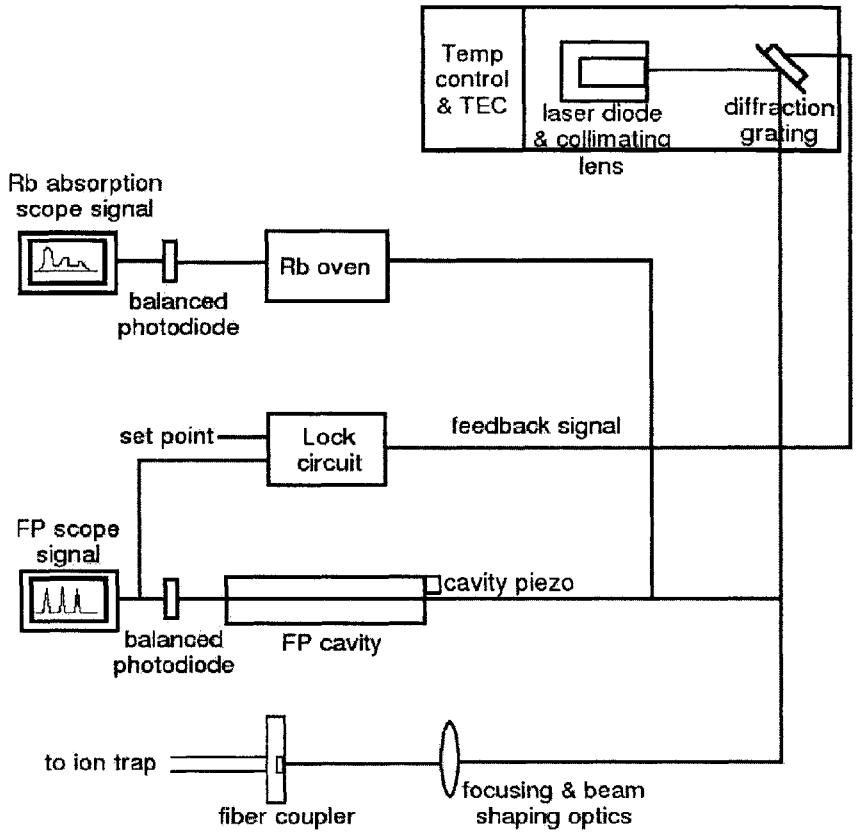

Figure 3-2: Blue laser schematic

Frequency measurement

Fortunately, the 422nm wavelength is very close to that of a transition in rubidium [MZNO94, MMB98], which we use as an atomic reference. The Rb absorption spectrum is obtained using a balanced photodetector by scanning the grating piezo, which sweeps the laser frequency. The spectrum observed consists of three peaks, of which the middle one is closest to the $^{88}Sr^{+}$ transition of interest.

Frequency stabilization

Diode lasers are very sensitive to changes in the diode current and temperature. These parameters are stablized by using a very stable current source and using a TEC to maintain a constant temperature of the diode box. Nevertheless, frequency drifts

are unavoidable, and lock circuitry is necessary. Part of the measurement beam is passed through a Fabry-Perot cavity. A photodiode measures the output beam that leaks from the cavity and sends it to a lock circuit. The lock circuit stabilizes the frequency by comparing this signal with a set point (side-locking) and adjusting the grating piezo and laser current to compensate to any drift. A cavity piezo glued to one of the mirrors of the cavity is used for precise tuning of the laser wavelength after locking. The 1092nm laser is almost identical in its design to the 422nm laser, except that the wavelength is measured using a wavelength meter.

The lasers can be tuned to the desired frequency using, in order of increasing fineness, the diode current, temperature, the voltage applied to the grating piezo and the voltage applied to the cavity piezo after locking.

Chapter 4

Cryogenic Ion Trapping

Unlike room temperature ion trapping, which is now a mature field, cryogenic ion trapping is still a developing technology. Although cryogenic trapping has been demonstrated with neutrals and ions in several experiments (c.f. Section 1.3.2), to our knowledge, the only prior effort that successfully observed chains of *single* atomic ions at 4K was the NIST mercury ion trap [PBIW96]. The goal of this chapter is to contribute to the field of cryogenic ion trapping by describing how to design and construct a long hold-time cryogenic trap for strontium ions that is loaded using laser ablation instead of the standard e-gun and oven technique used in traditional ion traps.

The outline of this chapter is as follows. In Section 4.1, we delve in more detail into the motivations for building a cryogenic ion trap that were mentioned briefly in Section 1.3.1. In Section 4.2, we describe the main parts of our cryogenic ion trap that are common to the different trapping experiments we conducted; the cryostat, the RF drive apparatus, the imaging system, and the optics for the cooling and ablation lasers. Finally, in Section 4.3, we describe general experimental techniques that are useful in our cryogenic ion trapping experiments. These can be grouped into design techniques that lower the pressure of residual gases and extend the hold time of cryogens, and laser ablation techniques for loading the ion trap.

4.1 Why build a cryogenic ion trap?

Most cryogenic ion traps built are built to increase the lifetime of a particularly reactive species. This is one of our motivations, but our quantum computation goal also makes cryogenic traps useful for several other reasons that are discussed below.

4.1.1 Residual gas pressure

Hydrogen is the predominant residual gas in room temperature UHV systems [Red03]. At higher pressures, the predominant gas is water vapor from exposure to air humidity. Both gases are reactive with typical elements used in ion trapping and chemical reactions are the main ion loss mechanism of ions cooled well below the trap depth.

An example of a hydrogen reaction that occurs frequently is the conversion of a Group II ion, X^+, to XH^+, which usually remains trapped since its charge to mass is very close to that of the original ion. In that case, the product can be identified using the spectral shift in the normal mode of two trapped ions in which one of them has undergone the reaction [Kin99]. Room temperature Sr^+ trapping experiments in our lab have seen this reaction occur at a rate of about once every ten minutes by observing an ion in a chain turn dark.

Using cryosorption, it is possible to pump hydrogen at any temperature below 20K [Hae89], and therefore hydrogen chemical reactions are not an issue in a cryogenic trap. In fact, the main residual gas in cryogenic trap is helium, an inert gas. Because of this, cryogenic traps can hold cold ions without reactive losses for months [G+91].

In traps whose depth is comparable to room temperature (25meV), ion loss can also occur via elastic collisions pushing the ion out of the trapping region. This is a particular problem for planar traps because of their shallow depth and has already been observed as a limiting factor on ion lifetimes in early planar traps [SHO+06]. The possibility of achieving very low gas pressures in cryogenic traps (less than 10^{-12} torr) as well as the lower energy of residual gas molecules reduces the rate of ion loss due to this mechanism. In quantum computation, the reduction of the elastic collision cross-section is even more crucial. Even if an elastic collision does not knock

an ion out of the trap, it still decoheres the qubit.

4.1.2 Heating rates

Two qubit gates make use of the motional state of the ions in a trap and hence, are sensitive to any heating of the vibrational state. A fundamental limit on heating rates in ion traps is thermal fluctuations (Johnson noise) in resistive trap electrodes and in power supplies. The spectral density $S_V(\omega)$ of voltage fluctuations in a resistive element is

$$S_V(\omega) = 4k_B T R(\omega) \tag{4.1}$$

where T is the temperature of the element and $R(\omega)$ is the real part of the complex impedance $Z(\omega)$ at frequency ω. This voltage fluctuation spectral density gives rise to fluctuations of the trapping electric fields, leading to a heating rate that varies as the inverse square of the distance between the electrode and the ion. With present traps, this heating rate, usually at the 1 quanta/s level is not important because it is dominated by other heating sources, but will eventually become important as traps are scaled down [LYS05]. By cooling an ion trap from room temperature to helium temperature, Johnson noise due to the trap electrodes is reduced by a factor of 75.

In current ion trap experiments, ion heating is dominated by an anomalous source of heating other than Johnson noise. In experiments where the trap size has been varied [T$^+$00], the results suggest that the heating rate varies as the inverse fourth power of the distance between the electrode and the ion. This scaling fits well with models of fluctuating patch potentials on the electrodes.

Deslauriers *et al* have conducted experiments in a needle trap where the distance between the electrodes could be varied to study the dependence of heating rates on trap dimensions [DOS$^+$06]. At room temperature, they observed the anomalous scaling behavior described above. The electrodes were then cooled to 150K by passing liquid nitrogen through them and they observed the scaling to change almost to that expected from Johnson noise, although the heating rate was still two orders

of magnitude higher. This experiment suggests that whatever the mechanism for anomalous heating is, it appears to be activated at a threshold temperature and can be expected to be quenched completely at 4K.

4.1.3 Interfacing with superconducting qubits

One exciting possibility opened up by putting an ion trap in a 4K environment is using superconductors. NIST's cryogenic trap uses a superconducting lead helical resonator immersed in the helium tank to drive the trap, obtaining a loaded Q of 3000 [PBIW96]. One other possibility is to make the trap electrodes out of a superconductor such as niobium.

Recently, there have been interesting proposals for combining ion trap qubits with superconducting charge qubits [TRBZ04, TBZ05]. A charge qubit is superconducting island connected to high resistance tunnel junction. Ion trap qubits have long lifetimes and thus make good memory units. On the other hand, charge qubits can be used to implement much faster nanosecond logic gates, and thus would be a good component in a processing unit. Swapping states stored different types of qubits can be achieved via the ion vibrational state. For example, to map the internal state of an ion to a charge qubit, a polarization dependent laser pulse couples the internal mode to the motional mode which then capacitively couples to the charge qubit. For increasing the coupling strength, a superconducting cavity can be used.

4.1.4 Practical concerns

There are other more practical reasons for building a cryogenic trap. To achieve a pressure low enough to have a reactive lifetime of a few hours in a room temperature trap, there are two requirements: (i) materials used in trap construction must be restricted to a small set of vacuum-compatible materials [Hal87] and (ii) the trap must be usually baked for a certain period of time to speed up outgassing. Typically, traps are baked at 150C or above, for times ranging from a few days to two weeks.

On the other hand, no materials outgas at 4K, so the choice of materials in

constructing traps becomes much wider. For example, we have used plastics and solder in our traps. The latter eliminates the need for spot-welding or ultrasonic soldering. Also, because baking is not necessary in a cryogenic trap, different trap prototypes can be tested with a fast turn-around time. This is particularly useful while testing a new design such as planar traps. For example, in a typical bath cryostat such as that employed in this thesis work, the cooldown time from room temperature to 4K is one day, and the warm-up time back to room temperature is another day, giving an overall turn-around time of two days.

4.2 The apparatus

Having described the motivations for building a cryogenic trap, we now proceed to describe our implementation. Although we have tested several traps over the course of our experiments, most elements of the apparatus besides the traps themselves are common to all experiments and will be described below.

4.2.1 The cryostat

The trap and related components are mounted on the 4K baseplate of a liquid helium bath cryostat (QMC Instruments, Model TK 1813) shown in Figure 4-1. The baseplate is heatsunk to the outside of a liquid-He reservoir (1.75 liters) that is surrounded by a 77K nitrogen shield.

Optical access to the inner vacuum chamber where the trap is mounted is provided by three windows on the side of the cryostat (Figure 4-1c) used for delivering laser beams and one window at the bottom of the cryostat used for ion imaging. There are two layers of windows: (i) an outer set at the room temperature shield whose purpose is simply to hold the vacuum in the cryostat while allowing optical access, and (ii) an inner set at the 77K shield whose purpose is to absorb 300K radiation and sink it into the nitrogen to increase the helium hold time.

For the outer set, we use $\lambda/10$ BK7 windows (Melles Griot, 02WBK226) with a wavelength cutoff at 2.9μm. The inner set windows are made by sandwiching a 1 inch

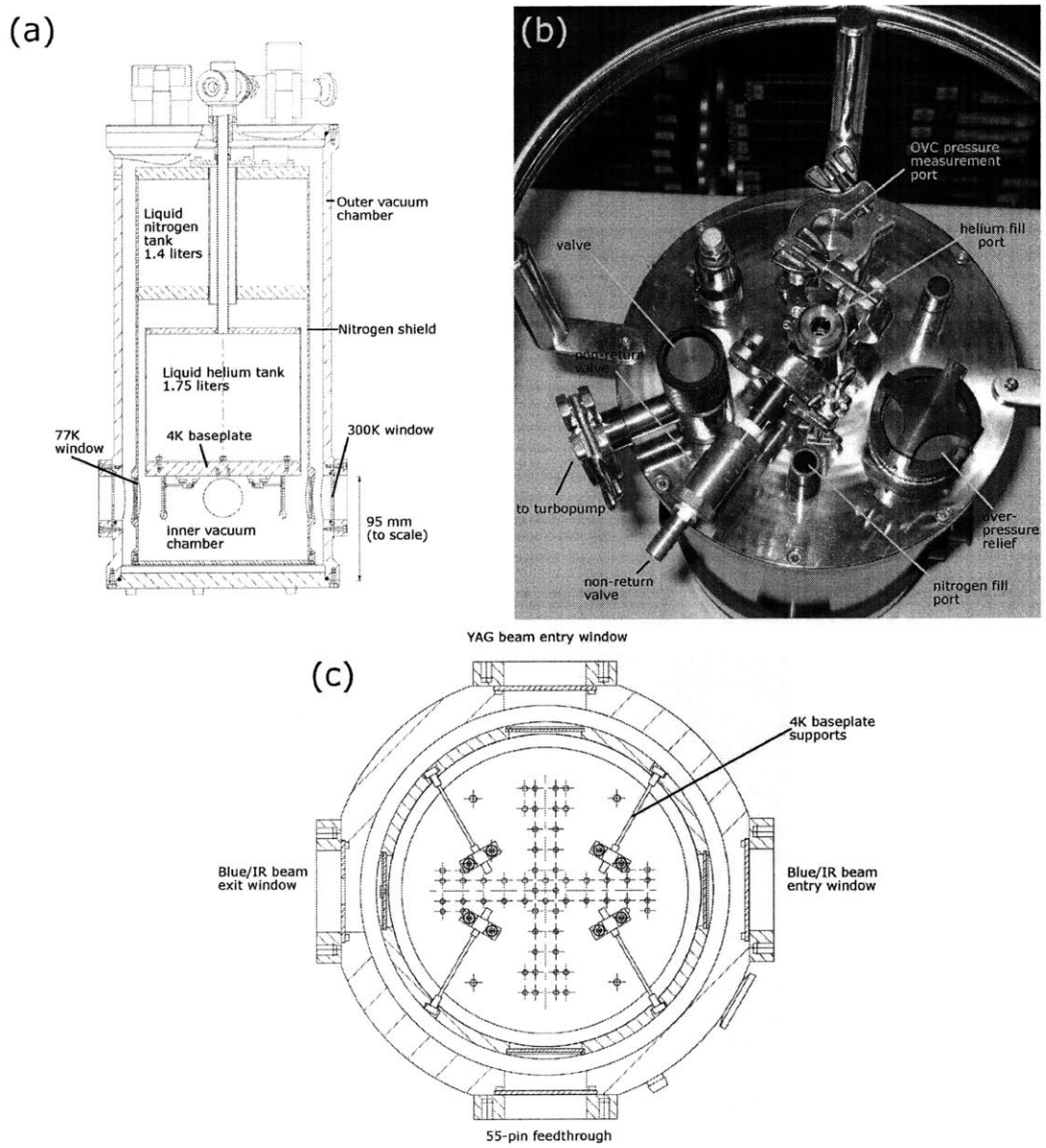

Figure 4-1: (a) Side view of the cryostat. (b) Fittings on the top of the cryostat including ports for filling the cryostat with cryogens, a port for pumping down the system and a port for attaching a pressure gauge to monitor the pressure in the outer vacuum chamber. (c) Helium baseplate (14cm diameter) and side windows of the cryostat. Figures (a) and (c) are adapted from [Ins].

BK7 window between two copper dics held together with screws. A pinhole is made in the copper dics whose size is as small as possible for the particular application. For windows passing laser beams, the pinhole is typically 1-2mm diameter, while a 24mm diameter hole is used for the imaging window. One on the copper dics is then anchored at the nitrogen shield with a layer of grease at the interface to enhance the thermal contact.

Two activated charcoal getters are mounted in the cryostat to increase the surface area for cryosorption, one at the top of the nitrogen shield and another on the helium baseplate. The getters each contain about 5g of charcoal enclosed in a copper container. Heating coils inside the getters are used for regenerating the getters.

To cool down the cryostat, we first pump it down to about $10^{-4} - 10^{-5}$ torr using a turbopump while running 0.08A through the heater coils to speed up the getter outgassing. About 12 hours later, we precool the cryostat by filling both its tanks with nitrogen. After another twelve hours, the helium tank is flushed using compressed helium and a helium fill is performed, typically taking around ten minutes. The cryostat is then ready for use.

4.2.2 RF drive apparatus

For trapping atomic ions in millimeter-scale traps like the ones we are using, the conditions of Mathieu stability and sufficient loading depth dictate that the RF drive have an amplitude of several hundred volts and a frequency of several MHz. The impedance mismatch between a commercial 50Ω amplifier and the much higher trap impedance usually makes driving the trap with an RF generator and amplifier very inefficient, and the reflected power from the trap can easily damage the amplifier. Instead, ion trappers usually use a particular realization of a quarter wave transmission line, known as a helical resonator, to obtain the voltage step-up.

Figure 4-2(a) is a schematic of our helical resonator. It consists of a coil whose length is chosen such that it is a quarter of the wavelength of the intended unloaded resonance. The coil is surrounded by a 3 inch diameter pipe for shielding. One end of the coil, known as the magnetic end, is grounded at the shield, while the other end,

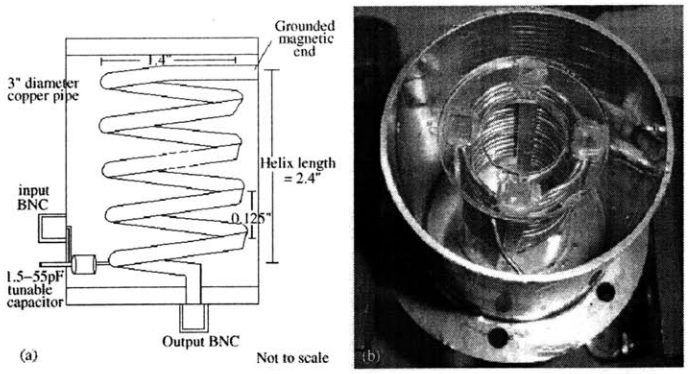

Figure 4-2: (a) Schematic of the resonator contruction. (b) Inside view of the resonator showing the bare copper coil wrapped around an acrylic support.

known as the electrical end, provides the high voltage output to the trap. The input is coupled at the electrical end through a high-Q tunable capacitor (1.5-55pF) that is also used for small adjustments of the resonant frequency.

We have found that our typical capacitive loads are around 30pF. The high capacitive load is mainly due to the cryostat feedthrough and wiring. The current drawn by the load is an important heat load on the cryostat and for future traps, which are likely to be run at even higher RF frequencies, we might need to use a resonator within the cryostat. The loading of the resonator drops its resonance frequency dramatically; the unloaded and loaded resonant frequencies of the resonator are 36 MHz and 7 MHz respectively.

We drive the resonator using an RF generator followed by a 50W RF amplifier. The resonator step-up is ≈ 20 and we are able to put up to 1kV amplitude on the trap, limited by arcing across trap electrodes. We measure the amplitude of the output using a calibrated antenna wire that runs in parallel with the resonator output wire for a distance of a few centimeters.

4.2.3 Ion detection

The detection of single ions requires careful design of the imaging optics and choice of the CCD. The requirements are good light collection and sufficient spatial resolution

for distinguishing the ions. To address the first requirement, we start by estimating the scattering rate of a single ion. An elementary quantum treatment [WMI+98] of the $^{88}Sr^{+}$ ion as a two level system excited by a laser beam with frequency ω_L and wavevector $\mathbf{k}_L$ yields the following formula for the photon scattering rate:

$$\Gamma_{sc} = \frac{\Gamma}{2} \frac{\Omega_R^2/2}{(\Delta\omega - \mathbf{k}_L \cdot \mathbf{v})^2 + \Gamma^2/4 + \Omega_R^2/2}, \tag{4.2}$$

where Γ is the natural linewidth of the 422nm transition, $\Delta\omega$ is the detuning of the laser, $\mathbf{v}$ is the velocity of the ion and Ω_R is the Rabi-frequency which determines the interaction strength and can be related to the saturation intensity

$$I_{sat} = \frac{2\pi^2 \hbar c \Gamma}{3\lambda^3} \tag{4.3}$$

as follows

$$\Omega_R^2 = \Gamma^2 \frac{I}{2I_{sat}}, \tag{4.4}$$

where λ and I are the laser wavelength and intensity respectively. For parameters used in our experiment, $\lambda = 422$nm, $\Gamma = 2\pi \times 22$MHz while I is typically ~ 20 mW/mm^2. This gives a maximum scattering rate of order 10^7 photons per second. Such high intensity makes observing a cloud easy, but for single ion detection, an intensity of order the saturation intensity is sufficient ($\sim 10\mu$W of blue).

It is convenient to put imaging optics such as lenses outside the cryostat. With these constraints, the dimensions of the inner vacuum chamber and imaging windows restrict the solid angle for light collection to $4\pi \times 0.016$ steradians. If we design our optics such that each ion occupies an area about 10 pixels, then we obtain $\sim 10^4$ counts per second per pixel assuming a CCD with high quantum efficiency at 422nm.

The CCD used in our setup (ST-3200ME, SBIG Astronomical Instruments) has 2184×1472 pixels with size 6.8μm. Its quantum efficiency at 422nm is 60%. The main source of imaging noise is laser scatter within the trap and is easily determined experimentally to estimate the necessary exposure time for obtaining a given SNR. In our case, for an exposure of 1s, we find the typical SNR for a single ion is ~ 10,

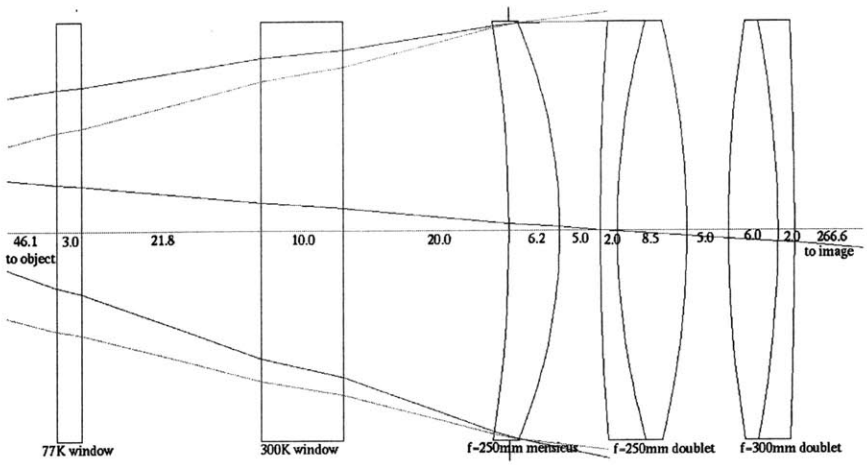

Figure 4-3: The lens system. The elements from left to right are: 77K window (OptoSigma, 044-1320), 300K window (Melles Griot, 02WBK226), meniscus lens (Thorlabs, LE1015), first achromatic double (Thorlabs, AC508-200-A1) and a second achromatic doublet (Thorlabs, AC508-300-A1). The spacings between elements given in the figure are in mm.

where the SNR is defined as

$$\text{SNR} = \frac{\max(\text{signal}) - \text{mean}(\text{noise})}{\text{standard deviation}(\text{noise})}. \tag{4.5}$$

Next, we estimate the necessary spatial resolution for observing single ions. At the crystallization point, the thermal and Coulomb energies of the ions are of the same order:

$$kT \sim \frac{e^2}{4\pi\epsilon_0 r}, \tag{4.6}$$

where r is the ion spacing and T is the ion temperature. We expect to easily Doppler cool the ions to 1K, corresponding to an ion spacing of a spacing of 16μm. The camera pixels are already small enough that a high magnification is not necessary, but the main challenge is to ensure that spherical aberrations do not lead to a larger than desired spot size.

Figure 4-3 shows the optics along the imaging path including the cryostat windows. We use two achromatic doublets and add a matched mensicus lens in front of the first

doublet to reduce its focal length without increasing the spot size significantly. We simulated the setup using OSLO (Lambda Research Corporation). The magnification is 2.54, while the resolved spot size is, in theory, limited by the camera pixel size to 2.7μm. In practice, we find the resolution to be limited by vibrations of the camera and the cryostat to 8μm.

4.2.4 Blue/IR laser delivery

The blue and IR lasers are delivered from the laser breadboards to the trap using optics fibers. The collimation packages on the output fiber couplers (Thorlabs, F230FC-A for blue laser and F230FC-C for IR) focus the beam so that the spot size at the waist is 150μm and 250μm for the blue and IR lasers respectively. The beams are coaligned with each other using a 45 degree cold mirror (Thorlabs, FM03) as shown in Figure 4-4. The blue/IR powers entering the cryostat are typically 400/500μW.

The beams are introduced into the cryostat along the trap's longitudinal axis. We have found Doppler cooling along the trap axis sufficient for obtaining ion crystals, but in future experiments where further cooling is required, it will be necessary to introduce the beams at a shallow angle relative to the axis to cool along the other principal axes.

4.2.5 YAG laser and optics

Our technique for loading the trap is laser ablation as described in Section 4.3.3. The ablation laser used is a Q-switched Nd:YAG (Minilite II, Continuum Electro-Optics) that produces 50mJ, 25mJ and 8mJ per pulse at its first (1064nm), second (532nm) and third (355nm) harmonics respectively. We use only the third harmonic for ablation loading. The pulse width is 3-5ns. The beam is focused down to a spot size of $\sim$ 1mm at the target.

Figure 4-5 shows the optics used for aligning and focusing the beam. Because this is a dangerous laser, the beam alignment is done in two stages. In the first stage, a rough alignment is performed by coaligning the YAG beam with a HeNe beam and

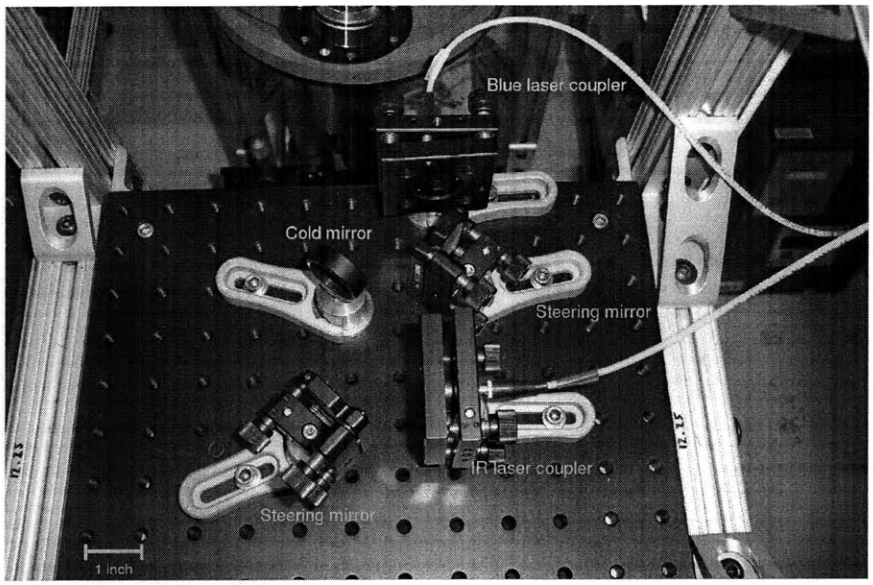

Figure 4-4: Optics for delivering blue and IR laser beams to the trap.

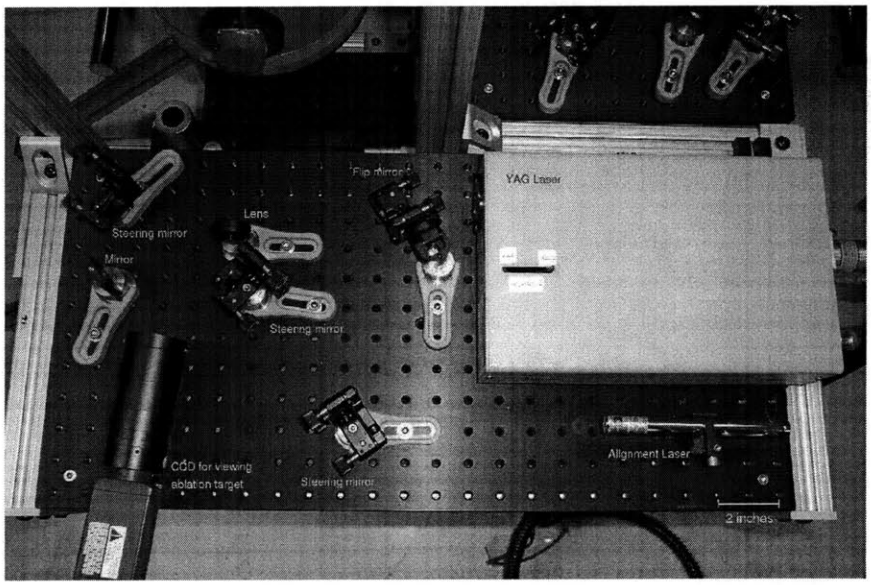

Figure 4-5: Minilite II ablation laser and associated optics for focusing and alignment of the beam.

then using only the HeNe for the rest of the alignment. This stage is particularly useful in more complicated setups than the one shown, for example, when the YAG beam is split to perform an ablation experiment with two targets. The second fine alignment stage is performed with the YAG laser in low power mode (1% of the full power) using a CCD to observe the beam scatter to move the beam spot to the desired position on the ablation target.

The steering mirrors used in the setup (CVI Laser, Y3-1025-45-P) also act as frequency filters by reflecting only the 3rd YAG harmonics. The power losses in the optics are low; the energy per pulse reaching the cryostat is measured using a pyroelectric meter (QE12-LP-S-MB, Gentec-EO) to be 6.9mJ.

4.3 Experimental techniques in cryogenic ion trapping

A large part of the the experimental design of a cryogenic ion trap goes into obtaining a low pressure within the cryostat and maintaining that pressure for a period of time long enough to conduct the desired experiments. This is the subject of this section. In addition, we also discuss ablation loading, which is partly motivated by the desire to increase the hold time of cryogens by avoiding traditional loading techniques that can contribute a large heat load.

4.3.1 Obtaining low pressures

The mechanism that produces an ultra-high vacuum environment in a cryostat is *cryopumping*, which is a generic name used for the production of vacuum by means of low temperatures. Cryopumping is the result of gas particles losing so much energy when they impinge on a cold surface that they become attached to it. Workers in the field categorize cryopumping into four distinct categories [Hae89]:

1. Cryocondensation: this is the normal condensation of a pure gas on a surface. The interaction responsible for it is the van der Waals' force between impinging

particles and particles that have already condensed. This mechanism restricts the partial pressures to be below the saturated vapor pressures of the component gases. At 4.2K, the gas with the second highest vapor pressure after helium is hydrogen, whose vapor pressure is 10^{-7} torr. All other gases have vapor pressures below 10^{-12} torr.

2. Cryosorption: porous solids such as activated charcoal or molecular sieves are used as adsorbents. The van der Waals' energy binding adsorbed molecules with the adsorbent is much higher than that in cryocondensation, making it possible to pump gases such as He and H_2 at 4.2K in subsaturated conditions, which results in partial pressures below the saturation vapor pressure.

3. Cryotrapping: used for pumping non-condensable gases by introducing a condensable gas whose crystallite surfaces adsorb the non-condensable gas molecules and incorporates them in the mixed condensate.

4. Cryogettering: relies on chemical bonding of active gases with metal films.

Of these mechanisms, only the first two play a role in our setup, with the second dominating the first because of the much larger adsorption energy. Our goal is to estimate the equilibrium partial pressures of the two main residual gases, hydrogen and helium.

We start by considering the pumping speed of the system, which can be taken to be that of the helium getter. The sticking coefficient, α, is defined in the literature as the fraction of the impinging gas particles that are adsorbed at a the cryosurface. A cryosorption pump has no constant pumping speed because α depends the fraction of a monolayer that has already been adsorbed, θ. α drops to zero when θ reaches 1. Nevertheless, experiments usually quote the value of α when $\theta \rightarrow 0$, which is the case in our crysotat as we shall soon see. Extrapolating the isotherms for the adsorption of helium on activated charcoal given by Gareis *et al* [GS67], we estimate the sorption capacity[1] of the helium getter at 4.2K and a He partial pressure of 10^{-11} torr to be 5×10^{-5} torr m^3.

[1]Sorption capacities are defined by convention at room temperature.

Given the volume of the cryostat, $\approx 0.015m^3$, and the fact that we turbopump it before cooling to at least 10^{-4} torr, dominated by the vapor pressure of water, our assumption of submonolayer coverage is justified. The pumping speed S (in particles/s) is then given by

$$S = \alpha n_g v_g/4 = \alpha p_g (2\pi m_0 k_B T_g)^{-1/2}, \tag{4.7}$$

where n_g is the gas number density, v_g is the mean velocity of the molecules, p_g is the gas partial pressure, m_0 is the mass of the molecules and T_g is the gas temperature. We assume T_g is 77K due to thermalizion with the nitrogen shield. Ozdemir *et al* [OP98] find the sticking coefficient of helium to activated charcoal to be around 0.2.

There are two main "leak" sources that determine the minimum pressure achievable in the cryostat. The first is desorption from the helium getter. Using Frenkel's law for the sojourn time of an adsorbed particle, the desorption rate, R_D is given by

$$R_D = \frac{N}{\tau_0} e^{-E_d/kT_S}, \tag{4.8}$$

where N is the number of adsorbed particles, E_d is the desorption energy per particle and T_S is the temperature of the cryosurface, and τ_0 is 10^{-13}s for most gases. To good approximation, N is the initial number of molecules of the particular gas before cryostat is cooled to 4K. For $\theta \rightarrow 0$, Edwards *et al* [EL78] cite a value of 30 for E_d/kT_S for helium.

The second leak source is real and virtual leaks that occur at a rate R_L. The outer shield of the cryostat is almost at room temperature and its outgassing contributes a virtual leak. For example, hydrogen continuously diffuses out of the grain boundaries of stainless steel. Helium diffuses through stainless steel and glass and contributes a real leak.

We can now estimate the equilibrium partial pressure of each gas as

$$p_g = \sqrt{2\pi m_0 k_B T_g}(R_D + cR_L)/\alpha, \tag{4.9}$$

where we have included a dimensionless conductance factor, c, that accounts for the low conductance between the outer vacuum chamber and the trap region. allows For hydrogen, since the getter temperature is well below its condensation temperature (20K), $R_L \gg R_D$, while the situation is reversed for helium.

Based on the figures cited in this discussion, we estimate the equilibrium partial pressure of helium in the cryostat to be $\sim 10^{-16}$ torr. Although lower pressures have been measured in cryogenic systems [G+91], this value is likely to be optimistic for our setup because of the introduction of laser beams into the crysotat. Scattered light from the beams causes light-induced helium desorption, which makes it difficult to achieve pressures much lower than 10^{-12} torr [WL95]. In addition, since the equilibrium partial pressure depends exponentially on E_d/kT, inaccuracies in the experimentally measured value of the desorption energy and the temperature of the charcoal can change our estimate of the pressure by up to 4 orders of magnitude.

Although the hydrogen partial pressure is expected to be lower than that of helium, it is the more important gas to study if we seek to increase the ion lifetime. To achieve that, we simply have to reduce the leak rate from the room temperature part of the cryostat. This could be done by putting the ion trap in a vacuum-tight pillbox, as has been done for example in the NIST cryogenic trap [PBIW96].

We have milled such a pillbox from oxygen-free copper as shown in Figure 4-6. Oxygen-free copper is chosen because of its very high thermal conductivity even at 4K; 20-100 $\mathrm{Wm^{-1}K^{-1}}$ depending on its residual resistivity ratio. The window layout corresponds to that of IVC and OVC and the windows are sealed using indium O-rings (ESPI, 0.040" 5N purity indium). A 50-pin D-sub cryogenic feedthrough (CeramTec, 16804-01-W) is used for introducing wires into the pillbox. The wires are thermally anchored by wrapping them several times around copper posts inside the box to reduce conduction of heat to the trap. The pillbox lid has pockets on both sides that are filled with activated charcoal and covered with copper mesh.

Using a turbopump, we could pump down the box to 10^{-5} torr. The box is then sealed using a copper pinchoff and transferred into the cryostat. Alternatively, a miniature normally closed solenoid valve can be installed for turbopumping the

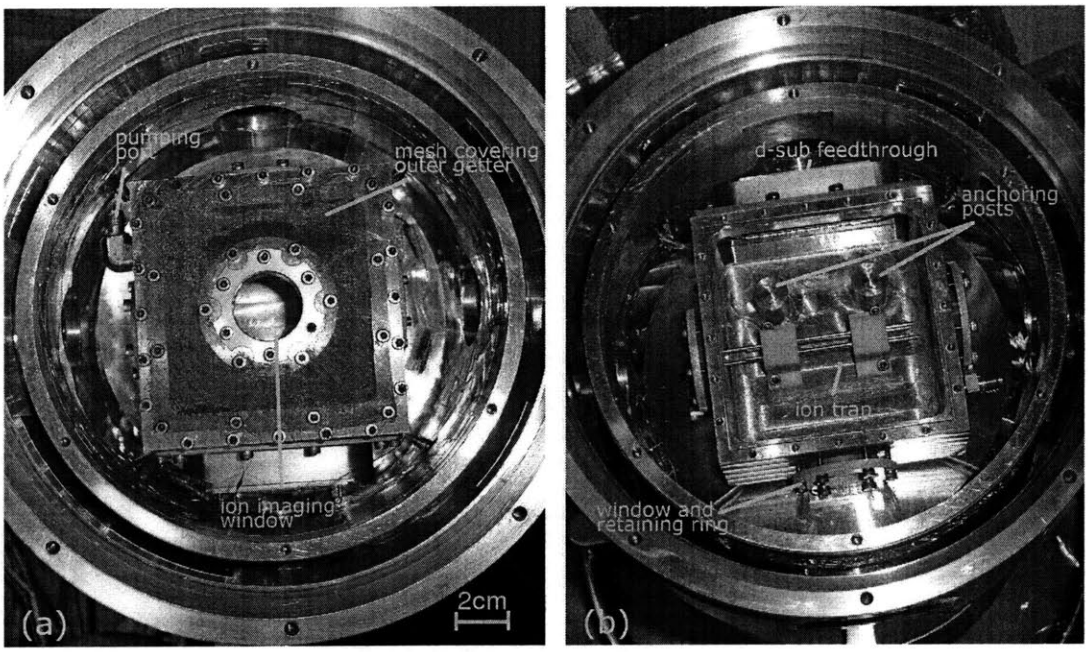

Figure 4-6: (a) Closed pillbox inside the crysotat. (b) A view inside the pillbox showing an early version of an ion trap installed in it.

pillbox along with the cryostat before closing the valve.

For our current experiments, we mount the trap in the cryostat without a pillbox. Future experiments that determine the ion lifetime will be conducted with and without the pillbox to determine the improvement in the hydrogen partial pressure that be obtained with this technique.

4.3.2 Increasing cryogen hold times

The reduction of the thermal heat load on a cryostat is an important design concern due to the very low latent heat of helium (20.4 J/g). We have measured the hold time for the cryogens in the absence of any heat loads introduced as part of the experiment, i.e. with metal blanks covering all windows to block thermal radiation and without any wires going into the cryostat.

A silicon diode temperature sensor (LakeShore, DT-471-SD) measures the temperature of the getter attached to the nitrogen tank. We find that the nitrogen tank

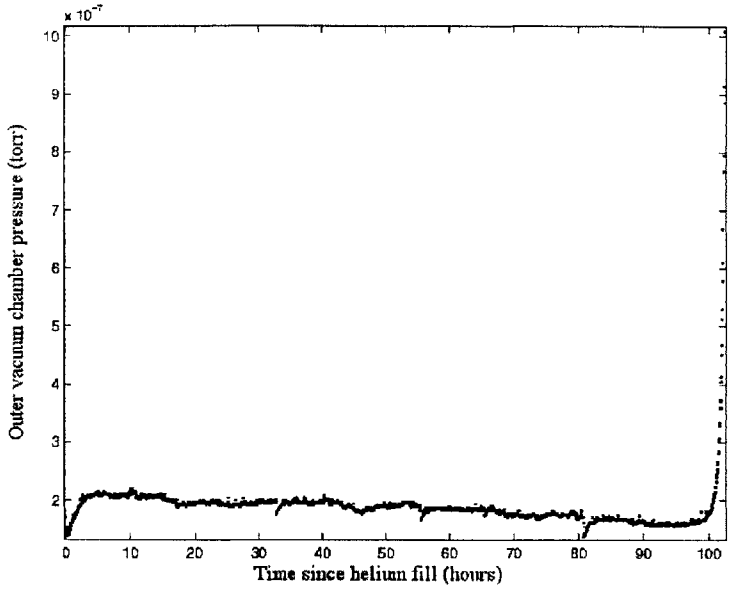

Figure 4-7: OVC pressure during a hold time measurement. Note the sharp rise of the pressure when the helium runs out and the dips in the pressure that occur when the nitrogen tank is refilled.

has to be refilled every 12 hours. For measuring the helium hold time, we monitor: (i) the pressure in the outer vacuum chamber using a wide-range gauge and (ii) the temperature of the helium baseplate using a ruthenium-oxide temperature sensor. The RuO sensor (LakeShore, RX-103A-AA) is greased with Apiezon N high vacuum grease and inserted into a hole drilled within a block of copper attached to the baseplate. Figure 4-7 shows a typical log of the outer vacuum pressure during a hold time measurement. Based on these measurements, we estimate the helium hold time, t_h, when the experiment introduces an extra heat load p as

$$t_h \text{ (days)} = \left(\frac{p \text{ (mW)}}{50} + 0.25 \right)^{-1} \tag{4.10}$$

The major contributors to the heat load p are: (i) blackbody radiation incident on the helium baseplate, (ii) conduction of heat from surfaces at a temperature higher than 4K through wires in thermal contact with the baseplate and (iii) resistive dissipation in these wires due to the flow of RF currents.

The energy flux, Φ, incident on the nitrogen shield is

$$\Phi = \epsilon \sigma T_r^4, \tag{4.11}$$

where σ is the Stefan-Boltzmann constant, $T_r = 300\text{K}$ and $\epsilon = 0.84$ is the emissivity of the radiation source, the BK7 300K windows. If this radiation is to simply enter through a "pinhole" of area 1cm^2, $\sim 40\text{mW}$ would enter the IVC and a large fraction of that power is likely to end up heating the helium. This illustrates the importance of the 77K windows. The pinholes in the copper windows are covered with BK7 as described in Section 4.2.1. For a small area pinhole, we can roughly model it as having a uniform temperature of 77K, assuming it is properly heat sunk to the nitrogen shield. The extra heat load introduced by the pinhole is then negiligible, $\sim 170\mu\text{W/cm}^2$.

For applying DC voltages to the trap, resistive dissipation is not an issue, so we use very thin (36AWG) phosphor-bronze wires (Lakeshore, WSL-36-500), which contribute on average about 0.5mW per wire to p. For introducing the RF, it is important to recall that the current only flows within a skin depth, δ, from the surface of the conductor:

$$\delta = \sqrt{\frac{\rho}{\pi f \mu}}, \tag{4.12}$$

where ρ is the resistivity of the conductor, μ is its permeability and f is the RF frequency. This is only $21\mu\text{m}$ in copper at 10MHz. Because of this, strip conductors are a good choice. In our case, we use a 5cm long strip of PCB substrate (FR4) that is covered with 1 ounce copper, anchored both 77K and 4K, which contributes a load of 2.5mW.

The RF dissipation in a strip of length l and width d covered with a layer of copper larger than the skin depth which is used to conduct RF of amplitude V and frequency f to capacitive load C is given by

$$\text{RF dissipation (mW)} = 5 \times 10^{-5} f^{5/2}(\text{MHz}) C^2(\text{pF}) V^2(\text{kV}) \frac{l(\text{cm})}{d(\text{mm})}. \tag{4.13}$$

For some of our typical trapping parameters ($V = 0.75$kV, $f = 8M$Hz) and a typical load capacitance (30pF, dominated by wiring to the trap), this gives a load of 11.5mW, ignoring losses in the trap and RF wires connecting it to the strip. Altogether these loads predict a helium hold time of about 1.5 days for a typical setup we use. Experimentally, we obtain a hold time of one day.

4.3.3 Ablation loading

Laser ablation is the removal of material by vaporization due to localized heating produced by an intense short pulse of light. The ablated material emerges as a plume consisting of neutral particles, ions and free electrons. Ablation has been previously used to load ion traps. Johnson and Kwong used it to load Al^+ in a cylindrical RF trap [JK84]. Knight used it to produce Be^+, Fe^+ and Pb^+ and store these ions in an electrostatic trap [Kni81]. Ablation has also been used in a cryogenic environment for loading neutral atoms, such as Cr and Mn, and small molecules, such as CaH, into magnetic traps [Wei02, deC03, Mic04].

A similar but distinct ionization technique, matrix-assisted laser desorption ionization (MALDI), is widely used by the mass spectroscopy community for the ionization of biomolecules [KBBH87, BCS89]. MALDI requires a secondary chemical matrix which holds particles of the substance to be ionized; in contrast, the laser ablation technique employed in this thesis work uses a target material with only the substance to be ionized.

Advantages of ablation loading

The traditional ion trap loading technique uses a resistively heated oven to produce neutral atoms that are ionized within the trap by bombardment with energetic electrons emitted from an e-gun. Laser ablation has several advantages over this technique, including some that make it particularly well-suited for a cryogenic traps and planar traps:

1. A typical oven/e-gun setup used in the room temperature experiments in our

laboratory dissipates at least 400J during each load (even to load a single ion!). Assuming ions are loaded only five times a day, we can translate this into a continuous average power dissipation of 23mW, which dwarfs all the other heat loads in the cryostat. By comparison, a single 8mJ ablation pulse can load a cloud with hundreds of ions.

2. Ablation loading is much faster than oven loading. Ablation plume dynamics are on the 1ms timescale while oven loading takes tens to hundreds of seconds.

3. The large electron flux from an e-gun accumulates on dielectric surfaces around the trap resulting in stray fields that change the compensation voltages for a trap on a day to day basis. By comparison, ablation loading produces a much smaller number of charged particles and we expect the compensation to remain fairly constant.

4. Ablation loading can be used to load very shallow traps such as planar traps. The minimum trap depth that we have managed to trap ions produced by laser ablation is 0.6eV, which is only slightly lower than what we measured for oven loading, 1eV. However, Kwong [Kwo89] has illustrated a technique where two plumes are created with perpendicular laser beams, timed such that the hot ions collide in the center of the ion trap, leaving some with nearly zero velocity.

5. In the long-term, ablation loading could be useful in quantum computation because, unlike an oven, it could be used for localized loading. As quantum computers are scaled up, ion loss, for example due to chemical reactions, will be an important error channel. In order to correct for such an error, the lost ion will need to replaced with a fresh ion. Therefore, it may be desirable to have many loading zones in the trap that can be quickly loaded with minimal perturbation to the rest of the trap by pointing the ablation beam at targets placed close to these zones.

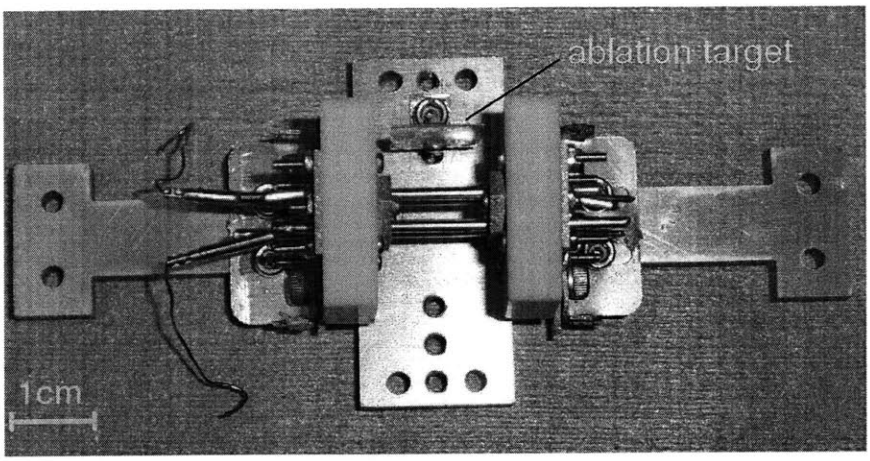

Figure 4-8: An ablation target in one of our earlier four-rod traps. This target is outside the trapping region and is at a distance of 7mm from the trap axis.

Target design

Ideally, we would use metallic strontium as the ablation target in our experiments. However, metallic strontium forms a layer a hydroxide layer in air, which makes target preparation outside the cryostat difficult. Instead, we use strontium (II) chloride which is deposited on a metal surface (copper or stainless steel) by rapid crystallization from its aqueous solution.

Specific target designs and positioning relative to the trap are given in the next two chapters, but in general, we have found that (i) we can load ions using targets within the trap (e.g. by coating the endcaps) and more surprisingly, using targets outside the trap, and (ii) a good position for the target is $\sim$ 10mm from the trap axis. Figure 4-8 shows an example of an ablation target mounted outside the ion trap. Another fact to keep in mind while choosing target orientation is that for a target that is smooth at the atomic level, e.g. a metallic target produced by evaporation, the ablation plume always comes out perpendicular to the surface, regardless of the angle of incidence of the ablation beam [And98]. However, larger angles of incidence produce less collimated plumes with less particles.

There are a few drawbacks to using strontium chloride instead of a metal target. We have found that a specific spot on the target is usually depleted within 10-30

shots, and the laser beam has to then be moved to a different spot on the target. This is the result of rather large clumps of $SrCl_2$ falling off the target (as opposed to being vaporized). Another drawback is that this powder tends to make trap surfaces dirty, particularly in the case of planar traps. This problem can be circumvented by putting the target far enough from the trap or using a mask with a pinhole.

4.4 Conclusions

We have demonstrated the design and construction of a cryogenic trapping apparatus for strontium ions. The hold time of the helium in the cryostat is one day, limited by RF dissipation in resistive elements of the trap and wiring. Based on cryopumping calculations, we expect the residual gas pressure in the cryostat to be below 10^{-12} torr. We expect our imaging system to be able to resolve chains of ions with a minimum ion separation of 8μm.

The main unique feature of our trap is the use of laser ablation for ion loading. We find that $SrCl_2$ targets placed about 10mm from the trap axis can be used as a reliable ion source for loading a trap using a single 8mJ shot of a tripled Nd:YAG laser.

Chapter 5

Cryogenic Knife-edge Trap

Loading an atomic planar trap, even a room temperature one, is a challenging problem in its own right. To decouple the challenges of cryogenic trapping from planar trapping, we used a four-electrode knife-edge trap for our first trapping experiments in the cryostat. With this trap, we verify that our non-conventional ablation loading technique works as expected and that the partial pressures of reactive gases in the cryostat are low enough so that ion lifetimes in an uncompensated trap are limited by RF heating rather than chemical reactions.

We begin this chapter by describing the design of our knife-edge trap in Section 5.1. In Section 5.2, we give the operating parameters of the trap. This is followed by some of the results obtained with this trap; in Section 5.3, we describe the observation of the cloud to crystal phase transition and in Section 5.4, we describe the observation of a chain of resolved single ions.

5.1 The knife-edge trap

In this section, we describe the mechanical aspects of our knife-edge trap, including the design of the compensation electrodes and the ablation target.

Figure 5-1 shows our three-segment linear Paul trap. This trap was designed and built by our collaborators in Japan who have used an almost identical trap with $^{40}Ca^{+}$ ions [FNTU05]. It consists of four 0.6mm thick stainless steel knife-edges whose cross-

section has a radius of curvature of 0.3mm. Two diagonally opposite electrodes are segmented into three segments. The middle segment, used as RF ground, has a length of 3mm and is separated from the outer segments by 0.5mm. The outer segments on each side of the trap are connected electrically and serve as endcaps. Unbalanced RF is connected to the other pair of diagonally opposite electrodes. These are unsegmented and have a length of 16mm. The electrodes are mounted on macor supports so that the distance r_0 between the trap axis and the closest electrode surface is 0.6mm.

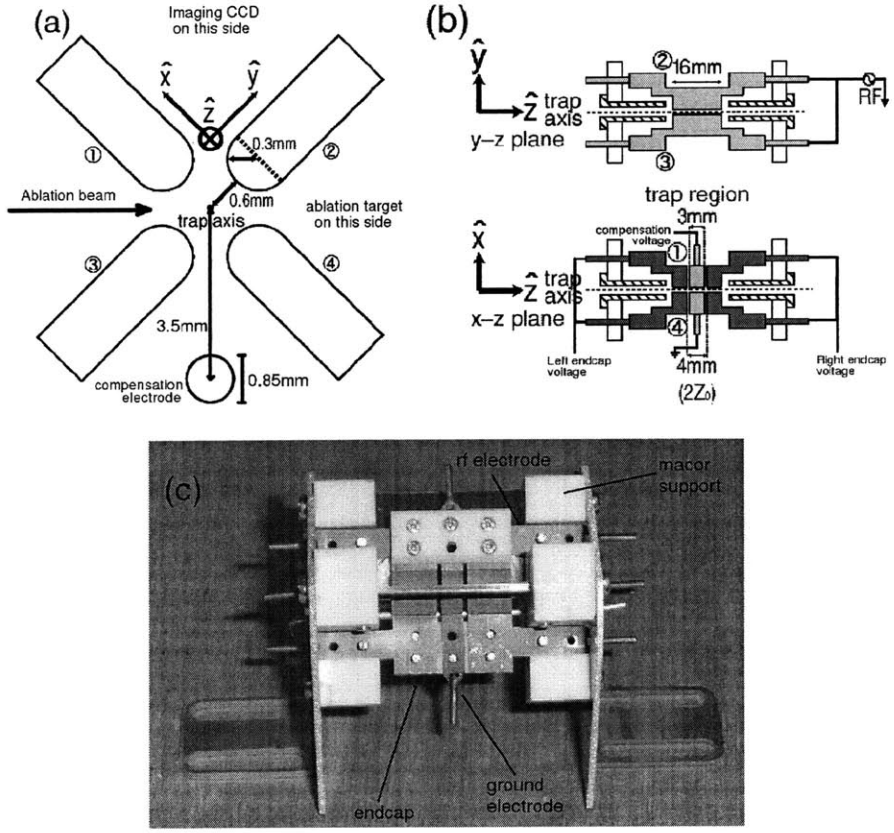

Figure 5-1: (a) Cross section through the trap. (b) View of the trap along two different planes that show the RF electrodes and the segmented ground/endcap electrodes. (c) A photograph of the trap. The trap electrodes are coated with Aquadag, an aqueous-based micro-graphite colloid that is used to reduce laser scatter. Figures (a) and (b) are adapted from reference [FNTU05].

Besides the electrodes used to generate the trapping potential, extra electrodes

have to be introduced to compensate stray static electric fields. A stray field $\mathbf{E}$ displaces the ion position by $\mathbf{u}$ whose components are

$$u_i \approx \frac{e\mathbf{E} \cdot \hat{\mathbf{u}}_i}{m\omega_i^2} \tag{5.1}$$

where $i = x, y, z$ and ω_i is the secular frequency in the ith direction. By Equation 2.6, this results in micromotion of amplitude $u_i q_i/2$ which cannot be reduced by laser cooling. Leakage of the micromotion from the radial directions to the axial directions can prevent resolving single ions if the amplitude of the driven motion in the axial direction exceeds the ion spacing in a crystal. We use two compensation electrodes to produce fields along independent radial directions. One of these electrodes is a rod placed 0.85mm from the trap axis as shown in Figure 5-1(a). The middle segment of one of the knife-edges is used as the other compensation electrode.

The ablation target is shown in Figure 5-2 in which the trap is seen mounted inside the cryostat. It is a copper piece with a right-angle cut that is coated with a layer of ~ 0.5mm of $SrCl_2$. The vertex of the right angle is 18mm from the trap axis and the two faces are used as two independent targets. The distances are chosen such that two plumes perpendicular to the targets would collide at the center of the trap.

5.2 Trap operation parameters

The trap is operated at an RF frequency of 7MHz. When loading, the RF voltage amplitude is 125V, corresponding to $q = 0.4$ and a depth of 6eV. After loading, we lower the RF voltage amplitude to 40V. The experiments reported in what follows only used a single target (c.f. Section 4.2.5 for ablation parameters). The ablation beam passes through the trap electrodes to hit the target. Unfortunately, the ablation plume is repelled by the field from the endcaps, but we find that we can get around that by starting with no voltage on the endcaps, triggering an ablation pulse and putting 25V on the endcaps 1s later.

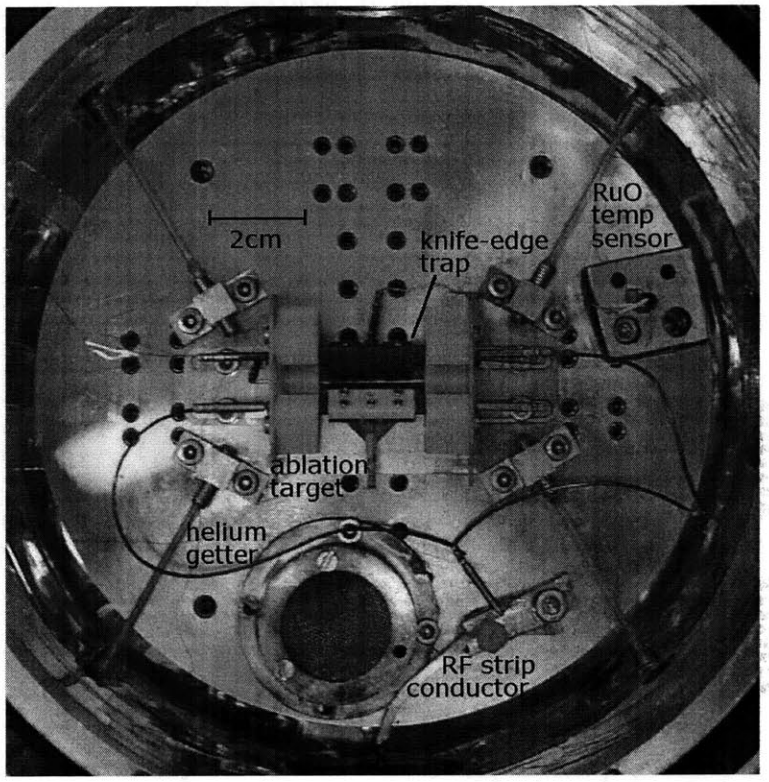

Figure 5-2: The knife-edge trap mounted inside the cryostat. The other items mounted on the baseplate are the helium getter, a copper block in which the ruthenium oxide sensor is inserted and the RF conducting strip.

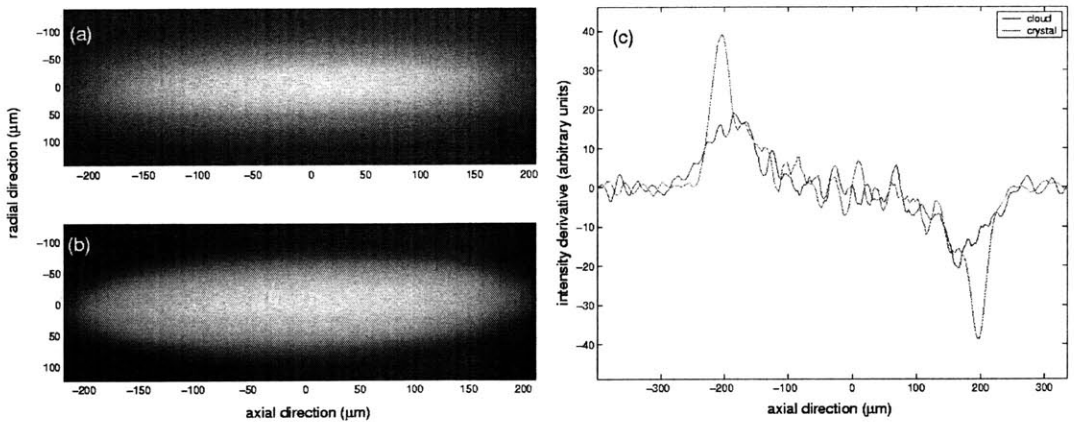

Figure 5-3: (a) A large cloud ($\sim$ 200μm wide) very close to crystallization, but still with blurred edges and (b) a crystal with sharper edges. (c) The derivative of the signal intensity along a cross-section through the axis of the trap shows the enhancement in the edge sharpness at crystallization.

5.3 Cloud to crystal transition in large clouds

As with most many-body systems with an interaction, a phase transition is expected [DPC+87] for a cloud containing a large number of ions when its temperature drops below a critical value; in this case, from a cloud to a crystal. The transition occurs when the Coloumb repulsion energy between the ions is of the same order as their kinetic energy. In a large cloud of ions, the ions cannot all line up along the RF null, and the displaced ions will heat up due to micromotion (RF heating). To induce the transition, the RF heating rate, which scales like V, can reduced by lowering the RF voltage, or the cooling rate can be increased by sweeping the cooling laser detuning from being far red-detuned (as it should be while loading ions) towards the atomic resonance.

The transition from a large cloud to a crystal can be identified in several ways including: (i) the formation of one of a variety of ordered states, e.g. concentric shells of ions, (ii) a dramatic increase in the scatter brightness when the crystal forms and (iii) an increase in the sharpness of the edges of a cloud.

Figure 5-3 shows the last effect in a typical transition we observed in our trap. This particular crystal was obtained via a combination of sweeping the 422nm and

1092nm lasers to the blue and lowering V from the loading voltage of 125V down to 40V. It is important to sweep both the cooling and repump lasers together so that they always address the same velocity groups. This is done by calibrating the cavity piezos of the blue and IR lasers so that the voltage to frequency conversion is known and then sweeping the lasers in the ratio of their frequencies. An initial starting point for the sweep is found by adjusting one of the lasers to obtain a Gaussian cloud profile along the axial direction. When the lasers do not address the same velocity groups, a dip is expected [ISN88] in the intensity at the center of the cloud as shown in Figure 5-4.

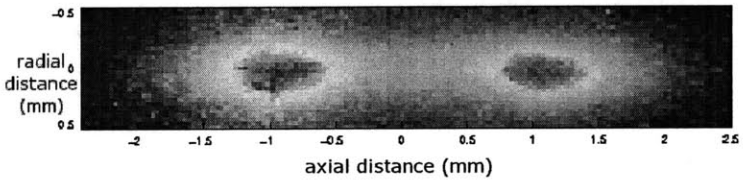

Figure 5-4: Non-Gaussian cloud fluorescence profile due to frequency mismatch between 422nm and 1092nm lasers.

5.4 Observation of single ions

Figure 5-5 shows a chain of resolved ions obtained in the knife-edge trap. An ion chain formed along the most weakly confining trap axis is the most energetically favorable configuration for a small number of cold ions when stray fields are compensated. To obtain an ion chain starting with a large ion cloud, we cycle through the following steps:

1. Lower the RF amplitude to reduce RF heating and reduce the trap depth. Reducing the trap depth helps reduce the number of ions in the cloud and also leads to evaporative cooling. Once the trap is properly compensated, the RF amplitude is increased again since RF heating is eliminated as a heating source.

2. Tune the 422nm and 1092nm lasers to the blue to maximize the ion signal.

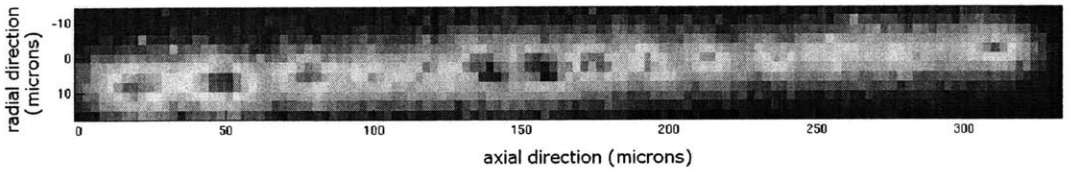

Figure 5-5: A chain of 14 ions in the knife-edge trap. The ion spacing is $\approx 27\mu$m.

If the lasers are tuned beyond the resonance, laser heating melts the crystal resulting in a sudden loss of intensity, but the melting is usually reversible.

3. Change the compensation voltages to bring the crystal closer to the RF null. This can be done in two ways: (i) by monitoring the enhancement in the crystal intensity, preferrably using a photomultiplier tube or (ii) by lowering the RF voltage, observing the direction in which the crystal moves and reversing that motion by applying the appropriate compensation voltages. The CCD should be refocused whenever the crystal is moved.

4. Lower the endcap voltages. In addition to reducing the number of ions in the trap, this also increases the spacing between ions in a crystal, making single ions easier to resolve.

The crystal in Figure 5-5 was obtained after lowering the RF amplitude from 125V to 75V, the endcaps from 25V to 0V and applying compensation voltages of 44V and 0.11V on the rod and ground segment compensation electrodes respectively. The compensation voltages provide us with an estimate of the typical stray fields in our trap, ~ 200V/m.

5.5 Conclusions

We have demonstrated trapping strontium ions in a cryogenic knife-edge trap, observing the cloud to crystal transition in large clouds and a chain of single resolved ions in a properly compensated trap.

There are two key extensions of this work. The first is the measurement of the reactive lifetime of the resolved ions, which should yield an estimate of the partial pressure of hydrogen, the main reactive gas in the cryostat. The second is the measurement of the total residual gas pressure in the cryostat, which we expect to be dominated by helium. One feasible technique for doing this would be to monitor the fluorescence signal from a few crystallized ions using a photomultiplier tube. The room temperature experiments in our lab have observed momentary dips in the fluorescence signal of such crystals which are attributed to a temporary decrystallization right after a collision with a residual gas molecule. The recrystallization time is determined by the cooling laser power, which has to be chosen carefully to allow for the detection of such dips.

Chapter 6

Cryogenic Planar Trap

In this chapter, we present the progress we have made towards designing, constructing, and operating a planar trap for atomic ions in a cryogenic environment. The inherent electrode asymmetry of such a trap makes 3D simulations of the trap potential necessary because dc voltages applied to control electrodes can displace ions from the RF null. In the absence of proper compensation for this displacement force, the resulting RF heating leads to very short cloud lifetimes, especially given the shallow depths of planar traps.

Inaccuracies of the simulation and stray fields remain problems that have to be experimentally addressed. Our solution is to experimentally compensate these fields using ion clouds that are collisionally cooled using a buffer gas.

The outline of this chapter is as follows. Section 6.1 describes the design of our planar trap for atomic ions and the results of simulations of its electrostatic potentials. Section 6.2 discusses our scheme for mounting the trap in the cryostat, designed to facilitate making a large number of connections to a small chip trap. Section 6.3 provides a model for studying the temperature of ion clouds loaded in the presence of a buffer gas and details the results of our experiments on buffer gas loading with a four-rod trap in preparation for using the same technique with a planar trap.

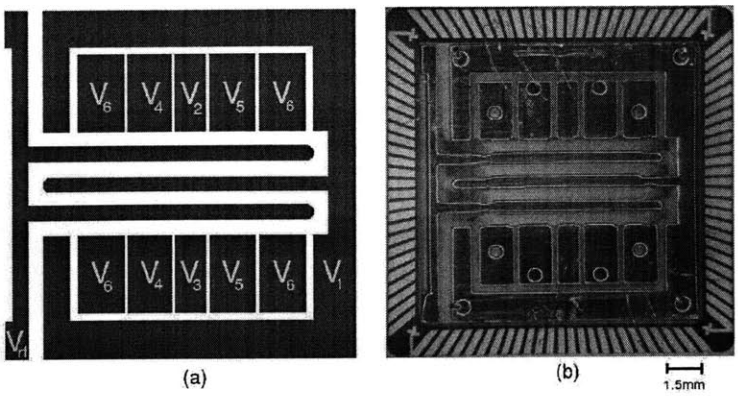

Figure 6-1: (a) Voltages applied to the trap. Identically labelled electrodes are shorted to each other. (b) Photograph of the trap in the CPGA. The RF and ground electrodes, as well as the slots between them, are 20 mils wide. The width of the middle pair of center electrodes is 30 mils and the rest have a width of 60 mils, with an inter-electrode spacing of 5 mils.

6.1 Trap design and simulations

In this section, we describe the design and trapping characteristics of our planar trap for atomic ions. Our trap, shown in Figure 6-1, is a second version of a PCB trap design that our lab has used to trap atomic ion clouds at room temperature [BCL+06]. The PCB was manufactured by Hughes Circuits using standard techniques. Like the macroscopic planar traps described in Chapter 2, it is a five electrode design: a center RF ground, two RF electrodes and two segmented outer electrodes that are used for endcaps and compensation. The copper electrodes are deposited on a low loss Rogers 4350B substrate. To reduce laser scatter into the CCD, we polish the electrodes using 1μm grit. The dielectric between the electrodes is milled out to avoid build-up of charge that can distort the potential close to the ion location.

We used a boundary element method electrostatic solver (CPO-3D, Scientific Inst. Serv.) to calculate the trap potentials. The voltages applied to electrodes are shown in Figure 6-1(a). In our simulation, we use $V_{RF} = 680$V amplitude at 6.8MHz, $V_1 = 10$V, $V_6 = 80$V and $V_i = 0$V for $i = 2, 3, 4, 5$. Thus, V_6 provides an endcap potential, but it lowers the ion location below the null, and this is compensated by V_1. The other electrodes are used for experimental compensation.

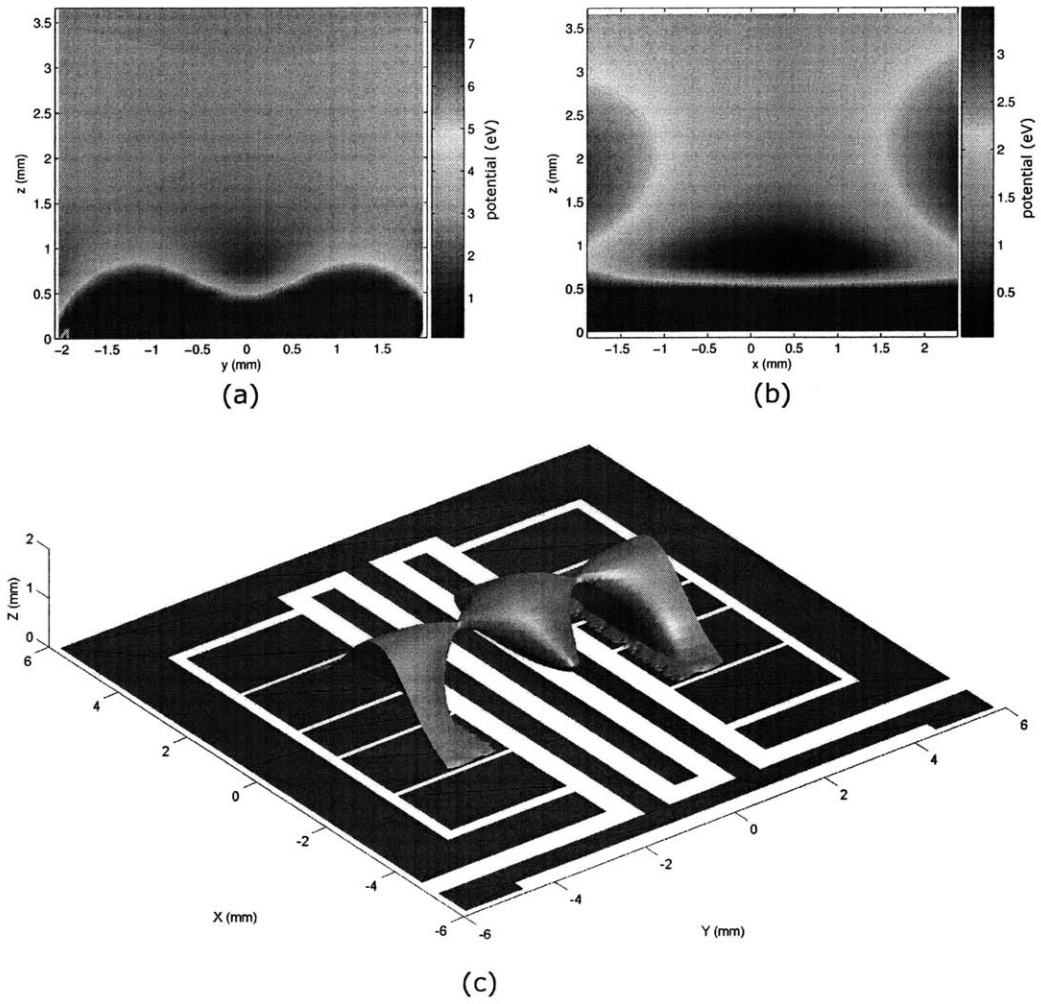

Figure 6-2: (a) Cross-section of the pseudo-potential in the $y - z$ plane at $x = 0$, (b) cross-section in the $x - z$ plane through $y = 0$, (c) isosurface of the pseudopotential at 1.33eV, slightly above the trap depth, showing the side-ways escape trajectory of the ions.

The calculated height of the ions above the trap surface is 0.86 ± 0.05mm. The depth is 1.3 ± 0.1eV and the secular frequencies are $\omega_x = 160 \pm 10$kHz, $\omega_y = 460 \pm 30$kHz and $\omega_z = 590 \pm 30$kHz, where our choice of coordinate system is indicated in Figure 6-2(c). The uncertainty in the secular frequencies is due to fitting the potential within an arbitrarily chosen range (one-tenth of the trap depth) to a parabola near the minimum of the anharmonic pseudopotential. The secular frequencies correspond to $q_y = 0.19 \pm 0.01$ and $q_z = 0.25 \pm 0.01$ for a harmonic trap.

6.2 CPGA mounting

As we scale down our traps, increase the number of electrical connections to them, and eventually switch to silicon traps, directly connecting wires to the trap becomes impractical. A better solution is to mount the trap on a CPGA chip-carrier (ceramic pin grid array) as shown in Figure 6-3(b). Lucent Technologies is also delivering its silicon traps mounted to an identical 100-pin CPGA (Global Chip Materials, Part No. PGA10047002). As per the pin assignment they provide, only fifty of the pins may be used for electrical connections.

We attach the trap described in Section 6.1 to the CPGA using a thermally conductive glue (Stycast Blue). For connections between electrodes and the gold pads of the CPGA, we use aluminum wirebonds. The CPGA is inserted into a socket that is thermally anchored to the helium baseplate as shown in Figure 6-3(a). Connections from the socket to the cryostat feedthrough are made, as before, using single phosphor-bronze wires.

Besides the trap and ablation target, we also attach to the CPGA pinholes to help in the alignment of the cooling beams and a threshold that prevents the YAG beam from accidently hitting trap components, such as the wirebonds, during alignment and damaging them.

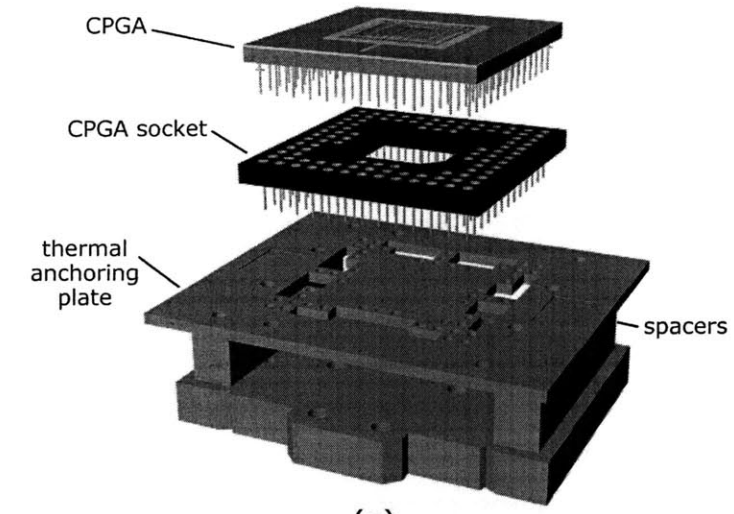

(a)

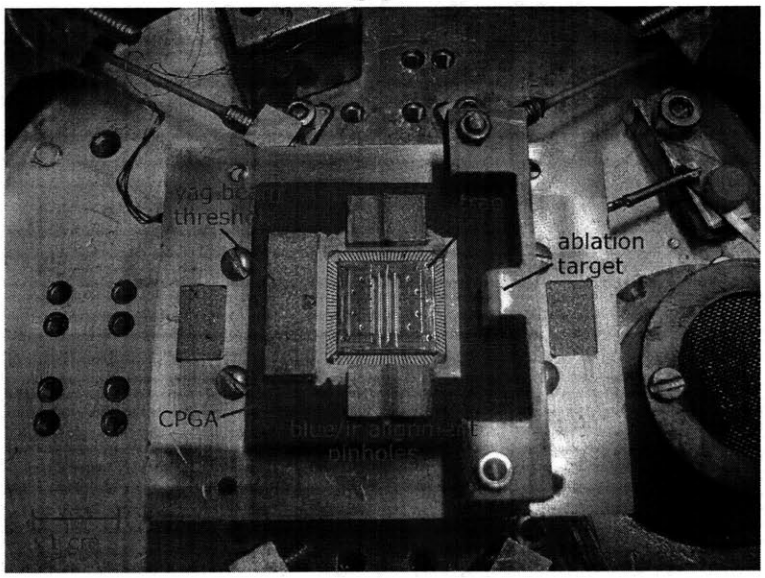

(b)

Figure 6-3: (a) CPGA mount parts: the CPGA chip-carrier is inserted into a socket that is thermally anchored to a copper plate by soldering the unused pins of the socket. The space underneath the plate is used for attaching wires to the socket. (b) Top view of the CPGA which shows the strontium ablation target and alignment pinholes.

6.3 Buffer gas loading

RF heating is a mechanism through which the RF trapping field can increase the temperature of an ion cloud. Normally, ion micromotion is in phase with the RF, so an ion gains and loses the same amount of kinetic energy during a cycle. However, when an ion has a collision with another ion or a residual gas molecule, it temporarily goes out of phase with the field and cannot give back its energy. This extra energy leads to an increase in the secular motion amplitude.

RF heating increases with the micromotion amplitude, which in turn increases as the ion is displaced from the RF null. This displacement can be due to stray fields, space charge repulsion in a cloud with a large number of ions or errors in the theoretical calculation of a compensated set of voltages. All three play a role in our planar traps, with the last exacerbated by the inability of CPO-3D to model dielectrics and the presence of surface charge on exposed dielectrics that we do not account for in our calculations.

It is well-established that the efficiency of Doppler cooling is very sensitive to the amplitude of micromotion [LBMW03, CGB+94, DHB89]. In the frame of motion of the ion, the laser frequency is modulated at the RF frequency, and photon absorption/emission can occur on these micromotion sidebands. Since we run our traps at about 8MHz, and the linewidth of the cooling laser is 22MHz, Doppler cooling is very sensitive to the laser detuning when the micromotion amplitude is large. In fact, in certain detuning ranges, the laser can heat the ions instead of cooling them [DHB89]. Only once an ion signal is observed can the detuning be experimentally optimized.

The large micromotion amplitude in a planar trap that is not experimentally compensated, the sensitivity of the Doppler cooling to the micromotion and the low depth of planar traps make loading a planar trap for the first time very difficult because of the extremely short ion cloud lifetimes. Following Brown *et al* [BCL+06], our approach to solve this problem is to load the trap with the aid of collisional cooling provided by He buffer gas, experimentally compensate the trap, and then load again in UHV.

Although the collisional cooling rate of buffer gas is higher than that of laser cooling, it also introduces a heating pathway of its own, namely neutral-ion collisions. It is important to have an estimate of the maximum stray field that can be tolerated for a trap of a given depth. Several theoretical models of buffer gas cooling exist in the literature [LBM92, VAVB83]; we extend the one used by Moriwaka *et al* [MTMS92] by introducing a stray field.

We use a Monte-Carlo simulation to obtain the equilibrium temperature of an ion cloud at different stray field magnitudes. Since we are after the steady state temperature, the initial conditions of an ion are of little interest besides determining the equilibriation time; we assume an ion's initial kinetic energy to be about the trap depth. The motion of the ion between collisions is determined by solving an inhomogeneous version of Equation 2.2

$$\frac{d^2x}{d\tau^2} + 2q\cos(2\tau)x = \frac{4eE_{dc}}{m\Omega^2}, \tag{6.1}$$

where E_{dc} is the magnitude of a stray electric field in the x-direction and to simplify the problem, we set $a = 0$. If the velocity of an ion right before the collision time, τ_c, is $\dot{x}(\tau_c)$, then after a head-on collision, it's velocity is

$$\dot{x}'(\tau_c) = \frac{(m - m_n)\dot{x}(\tau_c) + 2m_n v_n(2/\Omega)}{m + m_n} \tag{6.2}$$

where derivatives are with respect to τ and m_n and v_n are the mass and velocity of the neutral. Our neutrals are He atoms that are in thermal equilibrium with the 77K walls of the nitrogen shield of the cryostat. We assume that the pressure is high enough ($> 10^{-5}$ torr) that neutral-ion collisions dominate ion-ion collisions, so the latter can be neglected.

The mean kinetic energy at any time can be calculated by averaging over a secular period and subtracting away the contribution of excess micromotion due to the average displacement of the ion off the RF null

$$\bar{K} = \frac{1}{2}m(\bar{\dot{x}}^2 - (\Omega x_\mu)^2)(\Omega/2)^2. \tag{6.3}$$

Here x_μ is the micromotion amplitude determined using Equation 5.1.

We simulate 100 ion trajectories at each field magnitude. The results are shown in Figure 6-4. We see that the cloud reaches thermal equilibrium with the buffer gas typically within 10 collisions. The collision rate expected for a monopole-induced dipole interaction between the ion and the neutral is [Deh67]

$$\gamma = 2\pi n_n \left(\frac{\alpha_n e^2}{4\pi\epsilon_0 \mu}\right)^{1/2}, \tag{6.4}$$

where n_n is the He density, α_n is its polarizability and μ is the reduced mass of the ion and neutral. At a typical buffer gas pressure of 5×10^{-5} torr, this predicts an equilibriation time of about 10ms. To keep the temperature of the cloud below one-tenth of the trap depth, we find that the stray field magnitude has to be < 350V/m.

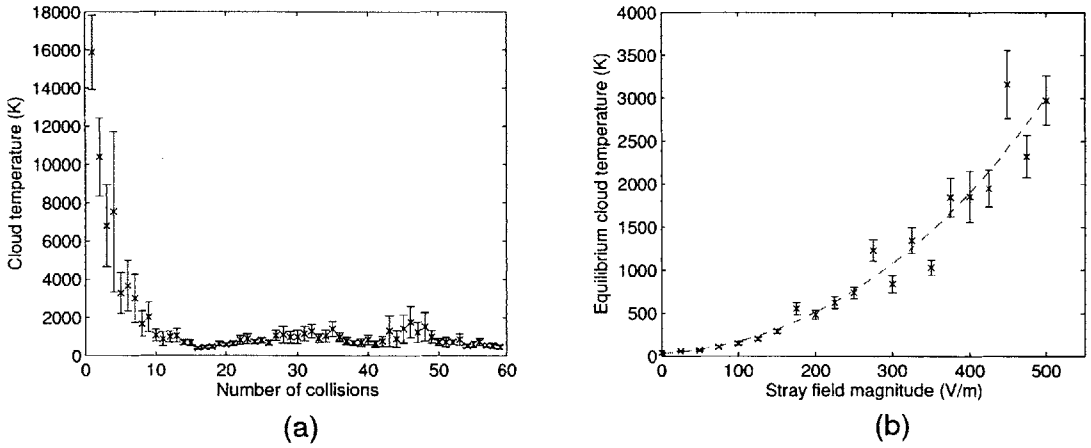

Figure 6-4: (a) Cloud temperature vs. the number of collisions with the buffer gas for a stray field of 225V/m. The simulation uses the y-secular frequency of our trap, but the results for temperature in the z-direction are similar. (b) Equilibrium cloud temperature for different stray field magnitudes. The dashed line is only to guide the eye.

Experimentally, He buffer gas cannot be used at 4K because it would be cryopumped by the getters until they are saturated. Instead, we introduce the He through a leak valve with the cryostat cooled to just 77K. The partial pressures of reactive gases are already low enough at that temperature (mainly hydrogen at 10^{-7}torr) so

we can obtain a sufficiently long reactive lifetimes to carry out compensation. We have tested this hypothesis by loading a 0.8eV four-rod trap with a buffer gas pressure of 5×10^{-5} torr and we obtained a lifetime of > 10 minutes. Experiments in progress are currently trying to load our planar trap in the same way.

6.4 Conclusions

In this chapter, we described a printed circuit board planar trap that we are currently trying to load with strontium ions. The compensated depth of this trap is 1.3eV. Based on experimental "simulations" of the planar trap using a four-rod trap, we found that this depth is sufficient for ablation loading in a compensated trap. However, because we expect rather large stray fields in the planar trap before compensation, we investigated loading in the presence of He buffer gas at 77K. Our model of buffer gas loading indicated that we can tolerate stray fields of up to 350V/m.

One improvement we would like to implement in a future version of our design of the CPGA mounting system for the trap is to use cryogenic ribbon cable to make connections. However, we expect the high resistance of the ribbon cable to cause a significant heat load on the cryostat due to RF pickup on the control electrodes. To address this, we will include a PC board between the CPGA socket and thermal anchoring plate that will incorporate RF filters close to the trap.

Chapter 7

Conclusion

In this thesis, we have presented experimental demonstrations of two ion trapping techniques that are interesting candidates for a large role in future large-scale trapped-ion quantum computers: planar traps and cryogenic trapping. Planar traps lend themselves to semiconductor microfabrication techniques, which will make it technically straightforward to manufacture multi-zone traps with a feature length-scale of order 100μm. Cryogenic trapping could reduce excessive heating rates due to this scaling and could eventually allow interfacing ion traps with superconducting qubits that are might be more suitable than ion qubits for certain quantum information applications.

Our macroscopic planar ion trapping experiments provide a first experimental demonstration of basic ion movement operations in this kind of trap, including ion shuttling, splitting and joining of ion chains and movement through intersections. Two techniques we have found useful in loading shallow traps are using an initial four-rod trap loading stage and adding a dc-biased electrode above the trap to increase the trap depth at the cost of increasing the micromotion.

Using our cryogenic setup, we have been able to observe single $^{88}Sr^{+}$ ions in a knife-edge trap. One of the most promising experimental techniques we have learned and demonstrated along the way is using laser ablation of $SrCl_2$ to load our traps. In addition to providing us with a fast, reliable way of loading our traps without an excessive heat load on the cryostat, laser ablation loading is particularly interesting

from a quantum information perspective because this loading technique has the potential for simplifying loading of ions into a localized, special-purpose "trapping zone" in a complex multi-zone trapped ion system.

We are currently working on loading a cryogenic planar trap with atomic ions, and based on experiments performed at room temperature with identical traps, we expect to demonstrate this soon. In the near term, our future experiments will focus on loading microfabricated silicon traps and characterizing their heating rates. Another future goal is to manufacture a trap using superconducting components such as niobium wires, and to use superconducting devices for electronic detection of the ion signal.

Ion traps are one of the most promising candidate physical systems for realizing a quantum computer. In the near future, the development of scalable, multiplexed traps and the reduction of decoherence rates in ion traps are likely to be high-priority research directions on the agenda of the trapped-ion quantum computing community. The work presented in this thesis provides some steps towards developing technologies that will hopefully help address these exciting challenges.

Bibliography

[AF86] S. Arnold and L.M. Folan. Fluorescence spectrometer for a single electrodynamically levitated microparticle. *Rev. Sci. Instrum.*, 57:2250–2253, 1986.

[And98] Z. Andreic. Time-integrated photographic study of laser ablation at large impact angles. *Fizika A*, 7:91–96, 1998.

[BCL+06] K. Brown, R. Clark, J. Labaziewicz, P. Richerme, D. Leibrandt, and I. Chuang. Micromotion compensation in a surface electrode ion trap. *arXiv:quant-ph/0603142*, 2006.

[BCS89] R. C. Beavis, B. T. Chait, and K. G. Standing. Factors affecting the ultraviolet laser desorption of proteins. *Rapid Commun. Mass Spectrom.*, 3:233–237, 1989.

[Ber02] D. Berkeland. Linear paul trap for strontium ions. *Rev. of Sci. Inst.*, 73:2856–2860, 2002.

[BZ88] R. Blatt and P. Zoller. Quantum jumps in atomic systems. *Eur. J. Phys.*, 9:250, 1988.

[Cam85] J. Camparo. The diode laser in atomic physics. *Contemp. Phys.*, 26:443–477, 1985.

[CBB+05] J. Chiaverini, R. B. Blakestad, J. Britton, J. D. Jost, C. Langer, D. Leibfried, R. Ozeri, and D. J. Wineland. Surface-electrode architec-

ture for ion-trap quantum information processing. *Quant. Inf. Comput.*, 5:419, 2005.

[CGB+94] J. Cirac, L. Garay, R. Blatt, A. Parkins, and P. Zoller. Laser cooling of trapped ions: the influence of micromotion. *Phys. Rev. A*, 49:421–432, 1994.

[CPK+02] Y. Cai, W.-P. Peng, S.-J. Kuo, Y. T. Lee, and H.-C. Chang. Single-particle mass spectrometry of polystyrene microspheres and diamond nanocrystals. *Anal. Chem.*, 74:232–238, 2002.

[CZ95] J. I. Cirac and P. Zoller. Quantum computations with cold trapped ions. *Phys. Rev. Lett.*, 74:4091, 1995.

[CZKM97] I. Cirac, P. Zoller, J. Kimble, and H. Mabuchi. Quantum state transfer and entanglement distribution among distant nodes in a quantum network. *Phys. Rev. Lett.*, 78:3221–3224, 1997.

[DBIW89] F. Diedrich, J. Bergquist, W. Itano, and D. Wineland. Laser cooling to the zero-point energy of motion. *Phys. Rev. Lett.*, 62:403–406, 1989.

[deC03] R. deCarvalho. *Inelastic scattering of magnetically trapped atomic chromium.* PhD thesis, Harvard University, 2003.

[Deh67] H. G. Dehmelt. Radiofrequency spectroscopy of stored ions i: Storage. *Adv. Atom. Mol. Phys.*, 3:53, 1967.

[Deu85] D. Deutsch. Quantum theory, the church-turing principle and the universal quantum computer. *Proc. of the Royal Soc. of Lond. A*, 400:97–117, 1985.

[DHB89] R. DeVoe, J. Hoffnagle, and R. Brewer. Role of laser damping in trapped ion crystals. *Phys. Rev. A*, 39:4362–4365, 1989.

[DHL+04] L. Deslauriers, P. C. Haljan, P. J. Lee, K-A. Brickman, B. B. Blinov, M. J. Madsen, and C. Monroe. Zero-point cooling and low heating of trapped $^{111}Cd^{+}$ ions. *Phys. Rev. A*, 70:43408, 2004.

[DiV00] D. DiVincenzo. The physical implementation of quantum computation. *Fortschritte der Physik*, 48:771–783, 2000.

[DOS+06] L. Deslauriers, S. Olmschenk, D. Stick, W. Hensinger, J. Sterk, and C. Monroe. Scaling and suppression of anomalous quantum decoherence in ion traps. *arXiv:quant-ph/0602003*, 2006.

[DPC+87] F. Diedrich, E. Peik, J. Chen, W. Quint, and H. Walther. Observation of a phase transition of stored laser-cooled ions. *Phys. Rev. Lett.*, 59:2931–2934, 1987.

[EL78] D. Edwards and P. Limon. Pressure measurements in a cryogenic environment. *J. of Vac. Sci. and Tech.*, 15:1186–1188, 1978.

[Els75] J. Elsey. Outgassing of vacuum materials. *Vacuum*, 25:299–306, 1975.

[Fey82] R. Feynman. Simulating physics with computers. *Int. J. of Theor. Phys.*, 21:467–488, 1982.

[Fis97] P. T. Fisk. Trapped-ion and trapped-atom microwave frequency standards. *Reports on Progress in Physics*, 60:761, 1997.

[FNTU05] T. Furukawa, J. Nishimura, U. Tanaka, and S. Urabe. Design and characteristic measurement of miniature three-segment linear paul trap. *Jap. J. of App. Phys.*, 44:7619–7624, 2005.

[FSL+95] P. Fisk, M. Sellars, M. Lawn, C. Coles, A. Mann, and D. Blair. Very high q microwave spectroscopy on trapped $^{171}yb^{+}$ ions: application as a frequency standard. *IEEE Trans. Inst. Meas.*, 44:113–116, 1995.

[G+91] G. Gabrielse et al. Cryogenic antiprotons: A 1000-fold improvement in their measured mass. *Am. Inst. Phys. Conf. Ser.*, 233:549, 1991.

[GC98] N. Gershenfeld and I. Chuang. Quantum computing with molecules. *Scientific American*, 278:66, 1998.

[GH02] C. G. Granqvist and A. Hultåker. Transparent and conducting ito films: new devolepments and applications. *Thin Solid Films*, 411:1, 2002.

[Gho95] P. K. Ghosh. *Ion Traps.* Clarendon Press, Oxford, 1995.

[Gor00] R. G. Gordon. Criteria for choosing transparent conductors. *MRS Bulletin*, page 52, August 2000.

[GS67] P. Gareis and S. Stern. *Cryog. Eng. News*, 26, 1967.

[H+05] W. K. Hensinger et al. T-junction ion trap array for two-dimensional ion shuttling, storage, and manipulation. *arXiv:quant-ph/0508097*, 2005.

[Hae89] R. Haefer. *Cryopumping: theory and practice.* Clarendon Press, Oxford, 1989.

[Hal87] B. Halliday. An introduction to materials for use in vacuum. *Vacuum*, 37:583–585, 1987.

[HB93] J. Hoffangle and R. G. Brewer. Frequency-locked motion of two particles in a paul trap. *Phys. Rev. Lett.*, 71:1828, 1993.

[HS03] J. P. Home and A. M. Steane. Electric octopole configurations for fast separation of trapped ions. *arXiv:quant-ph/0411102*, 2003.

[IBW87] W. M. Itano, J. C. Bergquist, and D. J. Wineland. Laser spectroscopy of trapped atomic ions. *Science*, 237:612, 1987.

[Ins] QMC Instruments. Standard TK1813 cryostat mechanical schematic. *www.terahertz.co.uk.*

[ISN88] T. Sauter I. Siemers, R. Blatt and W. Neuhauser. Dynamics of ion clouds in paul traps. *Phys. Rev. A*, 38:5121–5128, 1988.

[JK84] B. Johnson and H. Kwong. *Proc. 8th Int. Colleq. on UV and X-ray Spect. of Astrophys. and Lab. Plasmas*, page 163, 1984.

[JPM90] G. R. Janik, J. D. Prestage, and L. Maleki. Simple analytic potentials for linear ion traps. *J. Appl. Phys.*, 67:6050, 1990.

[K+05] J. Kim et al. System design for large-scale ion trap quantum information processor. *Quant. Inf. Comput.*, 5:515, 2005.

[KBBH87] M. Karas, D. Bachmann, U. Bahr, and F. Hillenkamp. Matrix-assisted ultraviolet laser desorption of non-volatile compounds. *Int. J. Mass Spectrom. Ion Process.*, 78:53–68, 1987.

[KBG+03] H. Klein, G. Barwood, P. Gill, G. Huang, S. Webster, P. Blythe, K. Hosaka, S. Lea, and H. Margolis. Trapped ion optical frequency standards. *Meas. Sci. & Tech.*, 14:1174–1186, 2003.

[Kie96] D. Kielpinski. *Entanglement and decoherence in a trapped-ion quantum register.* PhD thesis, University of Chicago, 1996.

[Kin99] B. King. *Quantum state engineering and information processing with trapped ions.* PhD thesis, University of Colorado, 1999.

[KMKP05] J. H. Kim, G. W. Mulholland, S. R. Kukuck, and D. Y. H. Pui. Slip correction measurements of certified psl nanoparticles using a nanometer differential mobility analyzer (nano-dma) for knudsen number from 0.5 to 83. *J. Res. Natl. Inst. Stand. Technol.*, 110:31, 2005.

[KMW02] D. Kielpinski, C. Monroe, and D. J. Wineland. Architecture for a large-scale ion-trap quantum computer. *Nature*, 417:709, 2002.

[Kni81] R. Knight. Storage of ions from laser-produced plasmas. *App. Phys. Lett.*, 38:221, 1981.

[Kwo89] V. Kwong. Production and storage of low-energy highly charged ions by laser ablation and an ion trap. *Phys. Rev. A*, 39:4451–4454, 1989.

[LBM92] M. Lunney, F. Buchinger, and R. Moore. The temperature of buffer-gas cooled ions in a paul trap. *J. of Mod. Optics*, 39:349–360, 1992.

[LBMW03] D. Leibfried, R. Blatt, C. Monroe, and D. Wineland. Quantum dynamics of single trapped ions. *Rev. of Mod. Phys.*, 75:281–324, 2003.

[LD98] D. Loss and D. DiVincenzo. Quantum computation with quantum dots. *Phys. Rev. A*, 57:120–126, 1998.

[LYS05] D. Leibrandt, B. Yurke, and R. Slusher. Minimizing ion trap thermal noise decoherence (unpublished). 2005.

[MCT+04] T. Metodiev, A. Cross, D. Thaker, K. Brown, D. Copsey, F. Chong, and I. Chuang. Preliminary results on simulating a scalable fault tolerant ion-trap system for quantum computation. 2004.

[Mee04] D. C. Meeker. Basic electrostatic analysis, version 1.0. http://femm.foster-miller.net, 2004.

[MHS+04] M. J. Madsen, W. K. Hensinger, D. Stick, J. A. Rabchuk, and C. Monroe. Planar ion trap geometry for microfabrication. *Appl. Phys. B*, 78:639, 2004.

[Mic04] R. Michniak. *Enhanced buffer gas loading: cooling and trapping of atoms with low effective magnetic moments.* PhD thesis, Harvard University, 2004.

[MMB98] A. Madej, L. Marmet, and J. Bernard. Rb atomic absorption line reference for single sr^+ laser cooling systems. *Appl. Phys. B*, 67:229–234, 1998.

[MTMS92] Y. Moriwaki, M. Tachikawa, Y. Maeno, and T. Shimizu. Collision cooling of ions stored in quadrupole radio-frequency trap. *Jpn. J. App. Phys.*, 31:L1640–L1643, 1992.

[MZNO94] M. Musha, A. Zvyagin, K. Nakagawa, and M. Ohtsu. Development of all-semiconductor laser sources for studies of $^{88}sr^{+}$ ions confined in rf trap. *Jpn. J. Appl. Phys.*, 33:1603–1607, 1994.

[NC00] M. Nielsen and I. Chuang. *Quantum Computation and Quantum Information.* Cambridge University Press, 2000.

[NF01] M. Nasse and C. Foot. Influence of background pressure on the stability region of a paul trap. *Eur. J. Phys.*, 22:563, 2001.

[NLR+99] H. C. Nägerl, D. Leibfried, H. Rohde, G. Thalhammer, J. Eschner, F. Schmidt-Kaler, and R. Blatt. Laser addressing of individual ions in a linear ion trap. *Phys. Rev. A*, 60:145, 1999.

[OP98] I. Ozdemir and D. Perinic. Helium sticking coefficient on cryopanels coated by activated carbon. *J. of Vac. Sci. and Tech.*, 16:2524–2527, 1998.

[OWN+02] K. Okada, M. Wada, T. Nakamura, I. Katayama, L. Boesten, and S. Ohtani. Cryogenic ion trap for minimization of trapped ion loss. *Jpn. J. Appl. Phys.*, 40:4221–4222, 2002.

[Pan76] M. Panish. Semiconductor lasers and heterojunction leds. *Proc. IEEE*, 64:1512, 1976.

[Pau90] W. Paul. Electromagnetic traps for charged and neutral particles. *Rev. Mod. Phys.*, 62:531, 1990.

[PBIW96] M. Poitzsch, J. Bergquist, W. Itano, and D. Wineland. Cryogenic linear ion trap for accurate spectroscopy. *Rev. Sci. Instrum.*, 67:129, 1996.

[PC04] D. Porras and J. I. Cirac. Bose-einstein condensation and strong-correlation behavior of phonons in ion traps. *Phys. Rev. Lett.*, 93:263602, 2004.

[PDM89] J. D. Prestage, G. J. Dick, and L. Maleki. New ion trap for frequency standard applications. *J. Appl. Phys.*, 66:1013, 1989.

[PLB+06] C. Pearson, D. Leibrandt, W. Bakr, J. Mallard, K. Brown, and I. Chuang. Experimental investigation of planar ion traps. *Phys. Rev. A*, 73:032307, 2006.

[Pre99] J. Preskill. Battling decoherence: the fault-tolerant quantum computer. *Phys. Today*, 52:24–30, 1999.

[R+02] M. A. Rowe et al. Transport of quantum states and separation of ions in a dual rf ion trap. *Quant. Inf. Comput.*, 2:257, 2002.

[Red03] P. Redhead. Hydrogen in vacuum systems: an overview. *AIP Conference Proceedings*, 671:243–254, 2003.

[RGB+92] M. G. Raizen, J. M. Gilligan, J. C. Bergquist, W. M. Itano, and D. J. Wineland. Linear trap for high-accuracy spectroscopy of stored ions. *J. Mod. Opt.*, 39:233, 1992.

[SCA+04] K. Svore, A. Cross, A. Aho, I. Chuang, and I. Markov. Toward a software architecture for quantum computing design tools. *Proceedings of QPL 2004*, page 145, 2004.

[SHKS01] M. Sawada, M. Higuchi, S. Kondo, and H. Saka. Characteristics of indium-tin-oxide/silver/indium-tin-oxide sandwich films and their application to simple-matrix liquid-crystal displays. *Jpn. J. Appl. Phys.*, 40:3332, 2001.

[Sho99] P. W. Shor. Polynomial-time algorithms for prime factorization and discrete logarithms on a quantum computer. *SIAM Rev.*, 41:303–332, 1999.

[SHO+06] D. Stick, W. Hensinger, S. Olmschenk, M. Madsen, K. Schwab, and C. Monroe. Ion trap in a semiconductor chip. *Nature Phys.*, 2:36–39, 2006.

[SS03] M. Sasura and A. M. Steane. Fast quantum logic by selective displacement of hot trapped ions. *Phys. Rev. A*, 67:062318, 2003.

[T+00] Q. A. Turchette et al. Heating of trapped ions from the quantum ground state. *Phys. Rev. A*, 61:63418, 2000.

[TBZ05] L. Tian, R. Blatt, and P. Zoller. Scalable ion trap quantum computing without moving ions. *Eur. Phys. J. D*, 32:201–208, 2005.

[Tho80] G. Thompson. *Physics of semiconductor laser devices.* Wiley, New York, 1980.

[Tho05] S. Thon. A 674nm external cavity diode laser for a $^{88}Sr^{+}$ ion trap. Bachelor's thesis, Massachusetts Institute of Technology. 2005.

[Tod91] J. F. Todd. Ion trap mass-spectrometer - past, present and future. *Mass Spec. Reviews*, 10:3, 1991.

[TRBZ04] L. Tian, P. Rabl, R. Blatt, and P. Zoller. Interfacing quantum-optical and solid-state qubits. *Phys. Rev. Lett.*, 92:247902, 2004.

[TWK+98] Q. A. Turchette, C. S. Wood, B. E. King, C. J. Myatt, D. Leibfried, W. M. Itano, C. Monroe, and D. J. Wineland. Deterministic entanglement of two trapped ions. *Phys. Rev. Lett.*, 81:3631, 1998.

[VAVB83] F. Vedel, J. Andre, M. Vedel, and G. Brincourt. Computed energy and spatial statistical properties of stored ions cooled by a buffer gas. *Phys. Rev. A*, 27:2321–2330, 1983.

[Wei02] J. Weinstein. *Magnetic trapping of atomic chromium and molecular calcium monohydride.* PhD thesis, Harvard University, 2002.

[WL95] P. Willems and K. Libbrecht. Creating long-lived neutral-atom traps in a cryogenic environment. *Phys. Rev. A*, 51:1403, 1995.

[WMI+98] D. J. Wineland, C. Monroe, W. M. Itano, D. Leibfried, B. E. King, and D. M. Meekhof. Experimental issues in coherent quantum-state manipulation of trapped atomic ions. *J. Res. Natl. Inst. Stand. Technol.*, 103:259, 1998.

[WO91] H. Winter and H. W. Ortjohann. Simple demonstration of storing macroscopic particles in a "Paul trap". *Am. J. Phys.*, 59:807, 1991.

[YF84] M. Yamashita and J.B. Fenn. Electrospray ion source: Another variation on the free-jet theme. *J. Phys. Chem.*, 88:4451–4459, 1984.

5000 - 2